BBSome-dependent ciliary Hedgehog signaling governs cell fate in the white adipose tissue

Katharina Sieckmann*[1], Nora Winnerling[1]*, Dalila Juliana Silva Ribeiro[1], Ronja Kardinal[1], Lisa Maria Steinheuer[2], Geza Schermann[3], Christina Klausen[1], Nelli Blank-Stein[4], Jonas Schulte-Schrepping[5], Collins Osei-Sarpong[5], Matthias Becker[5], Lorenzo Bonaguro[5], Marc Beyer[5,6], Kevin Thurley[2], Helen Louise May-Simera[7], Jelena Zurkovic[8], Christoph Thiele[8], Carmen Ruiz de Almodovar[3], Elvira Mass[4], Dagmar Wachten[1#]

[1]Institute of Innate Immunity, Biophysical Imaging, Medical Faculty, University of Bonn, Bonn, Germany
[2]Institute of Experimental Oncology, Biomathematics Division, University Hospital Bonn, Bonn, Germany.
[3]Institute for Neurovascular Cell Biology, University Hospital Bonn, University of Bonn, Bonn, Germany; Schlegel Chair for Neurovascular Cell Biology, University of Bonn, Bonn, Germany.
[4]Life and Medical Sciences (LIMES) Institute, Developmental Biology of the Immune System, University of Bonn, Bonn, Germany
[5]Platform for Single Cell Genomics and Epigenomics (Precise), German Center for Neurodegenerative Diseases and University of Bonn, 53127 Bonn, Germany
[6]Immunogenomics & Neurodegeneration, German Center for Neurodegenerative Diseases (DZNE), 53127 Bonn, Germany
[7]Institute of Molecular Physiology, Johannes Gutenberg-University, Mainz, Germany
[8]Life and Medical Sciences Institute, Biochemistry and Cell Biology of Lipids, University of Bonn, Bonn, Germany

*equally contributed
[#]corresponding author: Prof. Dagmar Wachten, Institute of Innate Immunity, BMZ-II, Venusberg-Campus 1, 53127 Bonn, dwachten@uni-bonn.de

Abstract

The primary cilium has emerged as critical in regulating whole-body energy metabolism, as reflected in the Bardet-Biedl syndrome (BBS), where primary cilia dysfunction leads to obesity due to hyperphagia and white adipose tissue (WAT) remodeling. The regulation of cell fate and differentiation of adipocyte precursor cells (APCs) is key to maintaining WAT homeostasis during obesity. Using mice that recapitulated the BBS patient phenotype (*Bbs8*$^{-/-}$), we demonstrate that primary cilia dysfunction reduces the stem-cell-like P1 APC subpopulation by inducing a phenotypic switch into a fibrogenic progenitor state, characterized by extracellular matrix (ECM) remodeling and upregulation of CD9. Single-cell RNA sequencing revealed a direct transition of stem-cell-like P1 cells into fibrogenic progenitors, bypassing the committed P2 cells. Ectopic ciliary Hedgehog signaling upon loss of BBS8 emerged as a central driver of the molecular changes in *Bbs8*$^{-/-}$ APCs, altering differentiation into adipocytes and lipid uptake. These findings unravel a novel role for primary cilia in governing APC fate, determining the delicate balance between adipogenesis and fibrogenesis. The identified molecular mechanisms provide insights into potential therapeutic targets for obesity.

Introduction

Obesity is a global challenge, affecting hundreds of million people worldwide and leading to metabolic disorders like type 2 diabetes, non-alcoholic fatty liver disease, and cardiovascular disease (Blüher, 2019; Boutari and Mantzoros, 2022). The white adipose tissue (WAT) drives obesity by tissue expansion upon excess energy intake, reaching up to 50% of body mass in severely obese humans (Das et al., 2003). Understanding WAT homeostasis and remodeling during obesity is paramount to mitigating the onset of these diseases. Various phenotypic changes have been observed in WAT upon fat accumulation: adipocyte function is disturbed, pro-inflammatory cytokines are secreted, leading to immune cells recruitment, activation, and, in turn, inflammation, and the extracellular matrix (ECM) remodels, leading to tissue fibrosis (Hasegawa, 2022). Remarkably, WAT persists as one of the few tissues harboring a significant reservoir of adult stem cells even in adulthood. These are mesenchymal adipose progenitor cells (APCs) that commit to the adipocyte lineage to form adipocytes, a process called adipogenesis (Rosen and MacDougald, 2006). In response to caloric imbalance, WAT dynamically adapts by generating new adipocytes through adipogenesis (hyperplasia) or by storing excess lipids in existing adipocytes (hypertrophy). Balancing these two processes is key to maintaining tissue homeostasis (Chouchani and Kajimura, 2019; Vegiopoulos et al., 2017; White, 2023).

Various signaling pathways have been shown to regulate the intricate process of adipogenesis and, thereby, WAT homeostasis (Ye et al., 2023). A pivotal player in this context is the primary cilium, a microtubule-based membrane protrusion that extends from the plasma membrane of most vertebrate cells. Primary cilia operate as a cellular antenna by sensing extracellular stimuli and locally transducing this information into a cellular response (Gopalakrishnan et al., 2023). Primary cilia originate from a modified mother centriole, the basal body that nucleates the microtubule-based ciliary axoneme. Protein transport in and out of the cilium is conveyed via the intraflagellar transport (IFT) machinery (Mill et al., 2023). Furthermore, the BBSome protein complex, formed by BBS proteins, functions as an adaptor for retrograde transport out of the cilium (Nachury, 2018), and the transition zone (TZ) controls lateral diffusion of membrane proteins at the ciliary base (Park and Leroux, 2022). Together, the IFT, the BBSome, and the TZ determine the protein composition of the primary cilium. Although the molecular composition of the cilium has only been determined for some cell types, it is already evident that a unique ciliary protein composition delineates the distinct response and function of a given cell type (Wachten and Mick, 2021).

Primary cilia are present on mesenchymal stem cells (MSCs) and cells committed to the adipocyte lineage, but are absent from mature adipocytes (Hilgendorf et al., 2019; Yanardag and Pugacheva, 2021). Genetic ablation of primary cilia in adipocyte progenitor cells (APCs) of adult mice completely inhibits adipogenesis (Hilgendorf et al., 2019). Furthermore, signaling pathways that engage the primary cilium have been shown to exert opposing effects on adipogenesis: for example, canonical Hedgehog (Hh) signaling, which is transduced via primary cilia, inhibits adipogenesis, whereas omega-3 fatty acids, which are sensed via the free fatty acid receptor 4 (FFAR4) in the cilium, promote adipogenesis (Hilgendorf, 2021). Thus, the presence of primary cilia is key for adipocyte development and WAT homeostasis, and ciliary signaling pathways play a dual role in controlling adipogenesis.

Primary cilia dysfunction leads to severe disorders commonly termed ciliopathies, some of which are associated with obesity. This includes the Bardet-Biedl syndrome (BBS), caused by mutations in one of the *BBS* genes, encoding for BBS proteins that are part of the BBSome or its associated protein complexes (Forsythe and Beales, 2013).

BBS mouse models recapitulate the human phenotype and develop obesity over time. At the cellular level, this seems to be due to dysfunction of primary cilia in hypothalamic neurons, leading to hyperphagia, accompanied by decreased locomotion and hyperleptinemia (Brewer et al., 2022; DeMars et al., 2023; Engle et al., 2021; Rahmouni et al., 2008). However, the development of obesity also seems to be driven by primary cilia dysfunction outside the central nervous system, as normalizing food intake to suppress hyperphagia also increases adipose tissue mass (Rahmouni et al., 2008). However, the molecular mechanisms, in particular the changes in ciliary signaling underlying WAT remodeling in BBS, are not known.

Recent breakthroughs in single-cell technologies have revealed that APCs are a highly heterogenous cell population. Based on gene expression analysis, lineage tracing, and surface marker expression (Altun et al., 2022; Scamfer et al., 2022), APCs include a stem cell-like, multipotent P1 subpopulation, a committed adipogenic P2 subpopulation, and different regulatory subpopulations, i.e., P3, also termed Aregs (Burl et al., 2018; Hepler et al., 2018; Merrick et al., 2019; Nahmgoong et al., 2022; Nguyen et al., 2021; Sarvari et al., 2021; Schwalie et al., 2018) (Fig. 1a). How the fate of these different subpopulations is determined at the molecular level is not well understood. Thus, it is important to shed light on APC complexity and diversity in terms of fate and function of the different subpopulations. Although the primary cilium and its associated signaling pathways have emerged as key regulators of adipogenesis, the cell-type specific role of primary cilia signaling in the different APC subpopulations, as well as the contribution to determining APC fate and function and, thereby, WAT homeostasis are completely unknown.

Here, we investigated the role of primary cilia in controlling fate and function of APC subpopulations in WAT under physiological conditions and during primary cilia dysfunction, i.e., in a BBS mouse model before the onset of obesity. Our results demonstrate that BBS8-dependent signaling determines the fate of APCs, in particular of the stem-cell like P1 subpopulation. Loss of the BBSome component BBS8 reduces the stem-cell pool by inducing a phenotypic switch of P1 cells into a fibrogenic progenitor subpopulation, characterized by ectopic ciliary Hh signaling and loss of Hh responsiveness. In turn, this affects the adipogenic potential of APCs and their lipid uptake. Altogether, our data demonstrate a key function for primary cilia signaling in determining APC fate and function in WAT, and provide mechanistic insights into phenotypic fate changes underlying cellular remodeling in tissue *niches* in ciliopathies, in particular BBS.

Results

Primary cilia control adipocyte precursor subpopulations. We first analyzed whether primary cilia are present on all APCs. Based on results by others, we established a flow cytometry antibody marker panel to identify and sort the different subpopulations from the stromal vascular fraction (SVF) of subcutaneous inguinal WAT (iWAT): After lineage depletion (Lin: TER119$^+$, CD45$^+$, and CD31$^+$, markers for erythrocytes, immune-, and endothelial cells, respectively) and selection of CD29$^+$ (Integrin β1) and SCA1$^+$ (stem cell antigen) APCs (Cho et al., 2019; Ferrero et al., 2020; Schwalie et al., 2018), we used the following markers to identify the APC subpopulations: CD55 (complement decay-accelerating factor) and CD26 (DPP4) for P1, CD54 (ICAM-1) for P2, and CD142 (tissue factor) for P3 (Fig. 1a-c, S1a) (Merrick et al., 2019; Schwalie et al., 2018). P1 was the most abundant APC subpopulation, followed by P2 and P3 (Fig. 1d). APCs of all three subpopulations displayed primary cilia with P1 showing the highest proportion of ciliated cells followed by P2 and P3 (Fig. 1e, f), whereas the cilia length was not different between the subpopulations (Fig. S1b). These results demonstrate that the proportion of ciliated cells is inversely related to differentiation towards committed adipocytes.

Next, we tested whether the different subpopulations maintain their *in vivo* characteristics when cultured *in vitro* for 48 hours. To determine the differentiation state of the different APCs, we analyzed FABP4 expression, an adipocyte commitment marker. Since it has been shown that regulatory P3 cells are resistant to undergoing adipogenesis, we focused on the P1 and P2 subpopulations (Schwalie et al., 2018). Only a few P1 but the majority of P2 cells were positive for FABP4 (Fig. 1g, h), indicating that P1 cells are not yet committed and more stem-cell like, whereas P2 cells are already committed to the adipogenic lineage, similar to what has been described *in vivo* (Merrick et al., 2019; Schwalie et al., 2018).

To investigate cilia-specific roles during adipogenesis, a minimal induction medium that allows to observe downstream effects of ciliary signaling is a prerequisite (Hilgendorf et al., 2019). Under minimal induction conditions alone, some P2 but none of the P1 cells differentiated into adipocytes (Fig. 1i, j), in line with P2 cells already being committed to the adipocyte lineage. To investigate the influence of ciliary signaling on adipogenesis, we stimulated the free fatty-acid receptor 4 (FFAR4), which has been shown to induce ciliary signaling and promote adipogenesis (Hilgendorf et al., 2019). In the presence of TUG-891, a FFAR4 agonist, both P1 and P2 cells strongly differentiated into adipocytes, even to the same extent as upon addition of a full induction cocktail (Fig. 1j). These results indicate that both P1 and P2 cells respond to a cilia-specific, adipogenic stimulus.

Loss of BBS8 results in obesity. To investigate whether primary cilia dysfunction, in particular loss of a BBS protein, affects fate and function of APCs, we used a mouse model that lacks BBS8 (*Bbs8*$^{-/-}$), a component of the BBSome complex (Tadenev et al., 2011). *Bbs8*$^{-/-}$ mice are lean until 10 weeks and then start to develop obesity (Fig. 2a). The gain in body weight is mirrored by an increase in all fat depot weights (Fig. 2b). We analyzed adipose tissue plasticity in further detail using our AdipoQ analysis pipeline (Sieckmann et al., 2022), which determines adipocyte size, determined by cell area, in a tissue section as well as the cell distribution within the tissue. We could show that the adipocyte cell size remains unchanged at 7 weeks, when the mice are lean, but it is increased in *Bbs8*$^{-/-}$ compared to *Bbs8*$^{+/+}$ mice at 15-17 weeks of age, when mice are considered obese (Fig. 2c-f). Thus, obese *Bbs8*$^{-/-}$ mice display adipose tissue hypertrophy (Fig. 2f). To investigate the contribution of the mesenchymal lineage and APCs to WAT remodeling, and as APCs are platelet-derived growth factor receptor α (PDGFRα) positive, we generated conditional knockout mice, lacking *Bbs8* in PDGFRα-expressing cells (*Pdgfra*$^{+/cre}$, *Bbs8*$^{flox/flox}$). Similar to the global in *Bbs8*$^{-/-}$ mice, these mice also developed obesity compared to control littermates (Fig. S2a), and their fat depot weights were increased at 17-21 weeks of age (Fig. 2g). When comparing the ratio of adipose tissue to body weight for the global and conditional knockout mice, we observed that the increase was similar for both (Fig. 2h), demonstrating that loss of BBS8 specifically in PDGFRα-expressing cells largely contributes to WAT remodeling and obesity development. In summary, loss of BBS8 leads to obesity due to adipocyte hypertrophy, which is driven by primary cilia dysfunction in PDGFRα-expressing cells.

Loss of BBS8 induces a fibrogenic switch and ECM remodeling. As we aimed to investigate the role of primary cilia in controlling APC fate and function independent of secondary effects due to obesity development, we focused our subsequent analyses to the 7-8 wks lean time point for all mouse models. To investigate the role of BBS8 in the P1-P3 APC subpopulations, we first compared their relative frequencies in the SVF from iWAT of lean *Bbs8*$^{+/+}$ and *Bbs8*$^{-/-}$ mice using the flow cytometry strategy described above. In comparison to *Bbs8*$^{+/+}$ mice, the P1 subpopulation in *Bbs8*$^{-/-}$ mice was significantly reduced, whereas the P2 and P3 subpopulations were slightly increased (Fig. 3a), indicating that lean *Bbs8*$^{-/-}$ mice harbor fewer stem cell-like APCs, which is recapitulated in the *Pdgfra*$^{+/cre}$, *Bbs8*$^{flox/flox}$ mice (Fig. S2b).

To investigate whether this change in frequency distribution resulted in functional defects, we sorted P1-P3 from *Bbs8*$^{+/+}$ and *Bbs8*$^{-/-}$ mice by flow cytometry and performed bulk RNA sequencing. According to the principal component analysis, overall gene expression was more similar in the P2 and P3 subpopulations and differed to that of P1 (Fig. 3b), which is also reflected in the marker expression. P1 displayed high *Creb5* (cAMP-responsive element binding-protein 5), *Ly6a* (lymphocyte antigen 5 family member A), and *Cd34* expression, P2 high *Pparg* (peroxisome proliferator-activated receptor gamma), *Fasn* (fatty acid synthase), and *Fabp4* (fatty acid binding-protein 4) expression, whereas *F3* (coagulation factor III), *Fmo2* (flavin-containing dimethylaniline monoxygenase 2), and *Rbp1* (retinol-binding protein 1) were enriched in P3 (Fig. 3c, S3a). When comparing the differentially expressed genes (DEGs, Tab. S1) in P1-P3 between *Bbs8*$^{+/+}$ and *Bbs8*$^{-/-}$ mice, the highest number of DEGs were observed in the P1 subpopulation, whereas the P3 subpopulations showed the least changes (Fig. S3b). This is further depicted in the volcano plots, showing the DEGs for each subpopulation (Fig. 3d, S3c-f). Gene ontology enrichment analysis of the DEGs in P1 revealed that predominantly genes associated with extracellular matrix (ECM) remodeling were up-regulated in *Bbs8*$^{-/-}$ mice (Fig. 3e), This included genes encoding for collagens (*Col1a1*, *Col3a1*, *Col5a1*, *Col6a1*) as well for ECM-regulating enzymes like *Loxl2* (lysyl oxidase-like 2), *Mmp3* (metalloproteinase-3), *Adamts2* (ADAM metallopeptidase with thrombospondin type 1 motif 2), and the laminin *Lama4* (Fig. 3f). We verified the increased expression of the ECM remodeling-associated genes by quantitative PCR (Fig. 3g). ECM remodeling has been implicated in controlling preadipocyte maturation and regulating stem-cell fate (Jääskelainen et al., 2023; Watt and Huck, 2013). During early commitment and differentiation, the fibrillar collagens (types I and III) are predominantly expressed, whereas a switch to basement membrane-associated collagens (types IV, VI, XV, XVIII) is associated with late differentiation (Jääskelainen et al., 2023). However, ECM remodeling is also a hallmark of tissue fibrosis, and excess ECM and fibrosis have been observed in WAT depots during obesity (Sun et al., 2023). The collagens that are upregulated during obesity in human and mouse adipose tissue (Jääskelainen et al., 2023) also include the collagens upregulated in lean *Bbs8*$^{-/-}$ mice under lean conditions. Altogether, primary cilia dysfunction upon loss of BBS8 results in a loss of the stem-cell like P1 APC subpopulation and an increased expression of ECM components.

Our data suggests that primary cilia dysfunction drives a fibrogenic, phenotypic shift in PDGFRα-expressing progenitor cells in WAT, which others have been associated with a shift from a CD9^{low} (tetraspanin-29) toward a *CD9*^{high} pro-fibrotic phenotype during obesity (Marcelin et al., 2017). We therefore analyzed CD9 expression in APCs from *Bbs8*$^{+/+}$ and *Bbs8*$^{-/-}$ mice by gating the CD9^{high} vs. CD9^{low} population in PDGFRα-expressing cells using flow cytometry (Fig. 3h, Fig. S3g). Strikingly, the frequency of the CD9^{high} subpopulation in

PDGFRα-expressing cells in the SVF was increased in *Bbs8*$^{-/-}$ compared to *Bbs8*$^{+/+}$ mice (Fig. 3h), demonstrating that loss of BBS8 induces a fibrogenic, phenotypic switch in P1 cells already in the lean state. To characterize the phenotype on a tissue level, we performed histological analysis, which also showed remodeling of the ECM in WAT from lean *Bbs8*$^{-/-}$ mice (Fig. 3i).

In summary, our data demonstrate that BBS8-dependent primary cilia signaling regulates the fate of the APC P1 population. Loss of BBS8 shifts P1 towards a fibrogenic phenotype, with enhanced fibrillar collagen synthesis and, thereby, WAT remodeling in the lean state.

Phenotypic switch of P1 cells impairs adipogenesis and promotes lipid uptake. To investigate whether the cilia-dependent phenotypic changes in *Bbs8*$^{-/-}$ APCs functionally affect APCs and impair adipocyte differentiation, we analyzed adipogenesis of APCs *in vitro*. It has been previously shown that the fibrogenic switch to CD9^{high} cells diminishes their adipogenic potential (Marcelin et al., 2017). To investigate whether a similar phenotype is also observed in the CD9^{high} population from lean *Bbs8*$^{-/-}$ mice, we performed *in vitro* differentiation in the presence of TUG-891, which promotes adipogenesis (Fig. 1j) (Hilgendorf et al., 2019). Our results demonstrate that the CD9^{high} population in *Bbs8*$^{-/-}$ mice does not respond to an adipogenic stimulus (Fig. 3j, k), as has been shown for CD9^{high} cells from obese mice (Marcelin et al., 2017). As the adipose tissue of *Bbs8*$^{-/-}$ mice expands via hypertrophy, we also analyzed whether the cell-intrinsic properties of lipid uptake are altered. To this end, we isolated P1 APCs from lean *Bbs8*$^{+/+}$ and *Bbs8*$^{-/-}$ mice, cultured and differentiated them *in vitro*, and fed the cells with alkyne-labeled fatty acids. Subsequent mass spectrometric analysis allows tracing of fatty acid incorporation into glycerolipids. Our results revealed that the synthesis of triacyl glycerides (TAG) is increased in *Bbs8*$^{-/-}$ compare to *Bbs8*$^{+/+}$ adipocytes (Fig. 3l). Altogether, these results show that the phenotypic switch in *Bbs8*$^{-/-}$ APCs diminishes their adipogenic potential and promotes fatty-acid uptake and, in turn, adipocyte hypertrophy.

Loss of BBS8 drives P1 cells towards a fibrogenic fate. To analyze the fibrogenic switch in more detail, we performed single-cell RNA-sequencing (scRNA-seq) of the iWAT SVF from lean *Bbs8*$^{+/+}$ and *Bbs8*$^{-/-}$ mice. Unsupervised clustering of the gene expression profiles identified the following known main cell types: APC P1-P3, fibroblastic progenitor cells (FPC), pericytes, endothelial cells as well as different immune cells (Fig. 4a, S4a), based on described markers for the different cell types and unbiasedly identified markers (Fig. S4b, c, Tab. S2). Since we observed a shift towards a fibrogenic phenotype in *Bbs8*$^{-/-}$, we focused on the APC subpopulations and the FPCs for the following analyses. The APC cell populations were characterized based on the expression of *Dpp4* (dipeptidyl peptidase 4) and *Pi16* (peptidase inhibitor 16) (for P1), *Col15a1* (collagen 15a1) (for P2), *Mmp3* (matrix metalloprotease 3) and *Bgn* (biglycan) (for P3) (Fig. 4b), as shown before (Merrick et al., 2019; Schwalie et al., 2018). Down-sampling to compare the abundance of cell populations between *Bbs8*$^{+/+}$ and *Bbs8*$^{-/-}$ mice revealed that the FPC abundance was increased in *Bbs8*$^{-/-}$ compared to Bbs8$^{+/+}$ mice (Fig. 4c, e, Fig. S4d, e). According to the Reactome analysis, the FPCs were characterized by a fibrotic signature, including an ECM remodeling signature (Fig. S4f), underlining the fibrotic phenotype observed in the tissue under lean conditions.

To investigate the cell-fate change at the single-cell level, we performed computational trajectory inferences on the P1-P3 subpopulations and the FPCs (Fig. 4f) using Monocle3. Pseudo-temporal analysis predicted, in line with previous data (Merrick et al., 2019; Schwalie et al., 2018), that P1 progenitor cells develop into P2 or P3 (Fig. 4f), and FPCs predominantly develop from P2 (Fig. 4f). By contrast, in *Bbs8*$^{-/-}$ mice, P1 cells preferably develop into FPC and then into P2 cells (Fig. 4f). Thus, these data further underline that loss of BBS8 results in a change in cell fate, with trajectory analysis supporting that P1 cells directly entering a fibroblastic precursor cell state with compromised ability to develop into P2 or P3.

A subpopulation of P2 cells preferably interacts with the WAT vasculature and their interactions are enriched in *Bbs8*$^{-/-}$ mice. A change in cell fate not only alters cell-autonomous functions, but also determines how cells communicate in the tissue *niche*. APCs interact with various cell types in the different WAT depots (Hildreth et al., 2021; Massier et al., 2023; Vijay et al., 2020). It has been described that the stem-cell like P1 APCs reside in the reticular interstitium/stroma between adipocytes (Merrick et al., 2019), while differentiation of committed precursor cells occurs along the vessels within the tissue in the perivascular *niche* (Gupta et al., 2012; Tang et al., 2008). As loss of BBS8 affects the differentiation trajectory of APCs, we wondered whether these changes also altered cell-cell interactions in the tissue. To this end, we applied CellChat (Jin et al., 2021), which identifies potential cell-to-cell molecular interactions, based on a database of ligand-receptor interactions, in scRNA-seq data. CellChat analysis showed a complex interaction map between the different APC populations, pericytes, endothelial cells, and fibroblasts when looking at the combined data from *Bbs8*$^{+/+}$ and *Bbs8*$^{-/-}$ mice (Fig. 4g). The three APC populations were the most active in sending signals to the other cells, mainly in their predicted interactions towards endothelial cells (Fig. 4g). Thus, we further characterized these cellular interactions with endothelial cells by sub-clustering (Tab. S3) and focused on the APC P2 subpopulation, which has been proposed to be close to the vasculature. We identified a subcluster in the P2 subpopulation, named APC P2_1 (Tab. S3), which showed the strongest potential interaction with the endothelial cells (Fig. 4h). The APC P2_1 subcluster was characterized by an enrichment for laminin and collagen ligands (Fig. 4i).

Strikingly, the stronger interaction was due to an increase in the collagen and laminin interactions, which were significantly increased in *Bbs8*$^{-/-}$ compared to *Bbs8*$^{+/+}$ mice (Fig. 4j). Altogether, our data indicate that loss of BBS8 leads to stronger interactions of the APCs, in particular P2_1, with the vasculature due to an increase in the expression of laminin and collagen ECM components. This suggests that primary cilia dysfunction in APCs not only causes a fibrogenic switch in the stem-cell like P1 APCs, but also alters the cellular interactions of committed APCs (P2_1) in the perivascular *niche* by ECM remodeling, which could further impact in the obesity phenotype.

Loss of BBS8 results in ectopic Hedgehog signaling and diminishes the Hh-dependent signaling response. To investigate the molecular mechanisms underlying the cilia-dependent change in cell fate, we analyzed primary cilia signaling in *Bbs8*$^{+/+}$ and *Bbs8*$^{-/-}$ APC cells in more detail. When analyzing the single-cell transcriptomics data, we observed that the Hedgehog (Hh) signature was increased in *Bbs8*$^{-/-}$ compared to *Bbs8*$^{+/+}$ APCs (Fig. 5a). Previous reports have shown that ciliary Hh signaling determines the fate of mesenchymal progenitor cells in skeletal muscle, the so-called fibro/adipogenic progenitors (FAPs) (Kopinke et al., 2021; Kopinke et al., 2017). FAPs promote differentiation of muscle stem cells and, thereby, muscle regeneration upon acute muscle injury. However, during chronic diseases, FAPs differentiate into adipocytes and produce fibrotic scar tissue. Ciliary Hh signaling in FAPs is maintained at a low level, but is strongly induced upon muscle injury, evoking a pro-fibrotic and anti-adipogenic response (Kopinke et al., 2021; Kopinke et al., 2017). In accordance with this finding, ectopic Hh signaling in FAPs upon loss of PATCH1 has been shown to evoke a pro-fibrotic and anti-adipogenic response (Norris et al., 2023). However, the role of ciliary Hh signaling in controlling a fibrogenic response in APCs of WAT remains unknown.

To test whether Hh signaling is affected in *Bbs8*$^{-/-}$ APCs, we analyzed the ciliary localization of SMO and the expression of Hh target genes. When stimulating Hh signaling using SAG, the ciliary SMO localization was significantly increased in both *Bbs8*$^{+/+}$ and *Bbs8*$^{-/-}$ APCs (Fig. 5b, c), indicating that the ciliary SMO relocalization is Hh-responsive in *Bbs8*$^{-/-}$ APCs. Intriguingly, under basal conditions, the ciliary localization of SMO was increased in *Bbs8*$^{-/-}$ compared to *Bbs8*$^{+/+}$ APCs (Fig. 5b, c), indicating that loss of BBS8 affects the localization of SMO in primary cilia. To investigate whether higher SMO localization affects downstream Hh signaling, we analyzed the expression of Hh target genes. Under basal conditions, the mRNA expression of *Gli1* and *Patch1* was higher in *Bbs8*$^{-/-}$ compared to *Bbs8*$^{+/+}$ APCs (Fig. 5d). Upon stimulation with SAG, the response was blunted in *Bbs8*$^{-/-}$ compared to *Bbs8*$^{+/+}$ APCs (Fig. 5e). These results were confirmed in MEFs from *Bbs8*$^{+/+}$ and *Bbs8*$^{-/-}$ mice: Under basal conditions, the ciliary localization of SMO was increased in *Bbs8*$^{-/-}$ compared to

Bbs8$^{+/+}$ MEFs and after stimulation with SAG, the ciliary localization increased in both genotypes (Fig. 5f). Downstream, the expression of *Patch1* was higher in *Bbs8*$^{-/-}$ compared to *Bbs8*$^{+/+}$ MEFs under basal conditions (Fig. 5g) and the response to SAG was dampened in *Bbs8*$^{-/-}$ (Fig. 5h). Thus, our results reveal that loss of BBS8 promotes basal ciliary SMO localization and, in turn, Hh downstream signaling. However, the response to stimulation of Hh signaling is dampened, making APCs unresponsive to Hh stimulation.

In summary, our results demonstrate that BBS8 regulates canonical Hh signaling in APCs of WAT to control APC cell fate.

Discussion

Tightly orchestrated commitment and differentiation of progenitor cells in the adipose tissue is key to maintain tissue homeostasis and function. Our study revealed that BBSome-dependent primary cilia signaling maintains the identity of APCs, specifically of the stem cell-like P1 subpopulation. In turn, primary cilia dysfunction in BBS results in ectopic Hh signaling, inducing a fibrogenic cell fate change that remodels the WAT. Our study adds a new chapter to how APC fate and function in WAT is maintained and regulated, and highlights the key role of primary cilia as a central regulator of tissue homeostasis.

BBS proteins control ciliary trafficking of GPCRs (Nachury, 2018; Wingfield et al., 2018), and SMO is one of the ciliary GPCRs whose ciliary trafficking is affected by loss of BBS proteins (Hey et al., 2021; Seo et al., 2011; Zhang et al., 2013). However, it remained largely unknown whether and how loss of a BBS protein alters ciliary signaling and, in turn, cellular functions, in particular during cell fate determination in the adult tissue. It has been shown that BBS7, another BBSome component, also controls the ciliary localization of SMO (Zhang et al., 2013). Furthermore, it has recently been shown that the fate of FAPs during skeletal muscle injury is controlled by Hh signaling and that loss of *Patch1* results in ectopic Hh signaling that changes the fate into a pro-fibrotic and anti-adipogenic state (Norris et al., 2023). Our results are in accordance with these findings and broaden the concept of how Hh signaling controls cell fate determination in the adult tissue. Our results indicate that ectopic activation of Hh signaling in WAT APCs induces a fibrogenic switch, reducing the pool of adipocyte progenitors and, in turn, the pool of cells that are key for tissue plasticity. Thereby, we link BBS and cell fate regulation by Hh signaling. Based on the results of FAPs in skeletal muscle and our results from APCs in WAT, this could be a general mechanism how BBSome-dependent primary cilia signaling controls cell fate determination of mesenchymal progenitor cells. Whereas Hh signaling controls FAP fate and function in a non-cell autonomous manner (Kopinke et al., 2017), loss of a BBSome component evokes a cell-autonomous action on APC fate and function. Thus, molecularly, BBS seems to mimic tissue injury, resulting in ectopic Hh signaling in the cilium and, in turn, a switch in cell fate. Of note, BBS proteins have also been proposed to play non-ciliary functions. For example, BBS proteins have been identified in the nucleus (Ewerling et al., 2023), where they seem to regulate gene expression (Gascue et al., 2012; Horwitz and Birk, 2021; Scott et al., 2017). Whether non-ciliary functions also play a role here, needs to be investigated in future studies. ECM remodeling in the adipose tissue is not *per se* pathological. In fact, ECM remodeling seems to be crucial for differentiation of a mesenchymal cell into an adipocyte, which undergoes dramatic morphological and cell size changes when storing triglycerides in lipid droplets (Jääskelainen et al., 2023). ECM remodeling occurs in the lean state upon feeding and is accompanied by an induction of lipogenesis (Toyoda et al., 2022). However, upon loss of BBS8, in the lean state, ectopic Hh signaling induces the fibrogenic switch, whereby the progenitor pool is reduced. Furthermore, also the committed P2 APC subpopulation seems to be affected by loss of BBS8. Here, the ECM remodeling also plays a role, whereby the interaction of a specific P2 subcluster, P2_1, with the ECs is increased. How this remodels WAT plasticity, needs to be further investigated.

The change in differentiation trajectory and remodeling of ECM in WAT of *Bbs8*$^{-/-}$ mice in the lean state is particularly interesting when considering that pathological ECM remodeling and fibrosis is a key driver of metabolic syndrome during obesity (Sun et al., 2023). *Bbs8*$^{-/-}$ mice develop obesity due to hyperphagia and WAT remodeling. The tissue displays hypertrophic expansion, which is underlined by our *in vitro* lipidomics analysis. Whether ciliopathy-induced, syndromic obesity is metabolically distinct from non-syndromic obesity needs to be investigated in future studies. Mice that lack the BBS chaperonin-complex protein BBS12 also develop obesity, but expand the adipose tissue by hyperplasia and retain normal glucose tolerance and insulin sensitivity (Horwitz and Birk, 2023; Marion et al., 2012). Whether this phenotype is due to primary cilia dysfunction in APCs or other cell types, is not known. Als studies in BBS patients suggests that the metabolic outcome in BBS patients might be distinct from patients with non-syndromic obesity (Picon-Galindo et al., 2022). Future studies will reveal whether components of primary cilia signaling in APCs are a suitable target to regulate WAT plasticity, advancing our understanding of metabolism and its associated pathophysiological mechanisms.

Methods

Animal Studies

All animal experiments were performed in agreement with the German law of animal protection and local institutional animal care committees (Landesamt für Natur, Umwelt und Verbraucherschutz, LANUV). Mice were kept in individually ventilated cages in the mouse facility of University Hospital Bonn (Haus für Experimentelle Therapie [HET], Universitätsklinikum, Bonn). Mice were raised under a normal circadian light/dark cycle of each 12 h and animals were given water and complete diet (ssniff Spezialdiäten) ad libitum (LANUV Az 81-02.04.2019.A170). Mice were sacrificed using cervical dislocation. Generation and breeding of *Bbs8*$^{-/-}$ mice and genotyping was previously described (Tadenev et al., 2011) and approved (LANUV Az 81-02.04.2019.A1428). Tissues and samples were collected from age-matched control (*Bbs8*$^{+/+}$) and mutant (*Bbs8*$^{-/-}$) littermates. The conditional mouse line has been generated based on the line C57BL/6N-Ttc8tm1a(KOMP)Wtsi/MbpMmucd, stock number 050244-UCD (MMRRC). Mice have first been crossed to Flp^{e} mice (Rodriguez et al., 2000) to generate *Bbs8*$^{flox/flox}$ mice and then to *Pdgfra*$^{+/cre}$ (Krueger et al., 2014) mice (JAX 013148) to generate *Pdgfra*$^{+/cre}$, *Bbs8*$^{flox/flox}$ mice.

Adipose tissue progenitor cell isolation

Progenitor cell isolation from the stromal vascular fraction (SVF) was performed as previously described (Sieckmann et al., 2022). Briefly, inguinal WAT was surgically removed, minced, and digested with 2 mg/mL collagenase II (Life Technologies) and 15 kU/mL DNAse I (PanReac AppliChem) in 0.5% bovine serum albumin (BSA; Sigma) in phosphate-buffered saline (PBS) at 37°C with agitation. The digestion was quenched by adding AT buffer (0.5% BSA in PBS). The dissociated cells were passed through a 100-μm filter (Corning) and subjected to centrifugation at 500 × *g* for 10 min. The resulting supernatant containing mature adipocytes was aspirated, and the pellet, consisting of the stromal vascular fraction, was resuspended in red blood cell lysis buffer (BioLegend) for 2 min at RT. The reaction was stopped by adding AT buffer and centrifugation at 500 × *g* for 10 min. Isolated cells were then further subjected to antibody staining for MACS or FACS processing.

Isolation and Immortalization of mouse embryonic fibroblasts

For the isolation of mouse embryonic fibroblasts (MEFs), timed matings were set-up with one male and two females of the desired genotype. At day 13, the pregnant mouse was anesthetized using isoflurane (Piramal Healthcare) followed by a cervical dislocation. The lower abdomen was opened by an abdominal incision to extract the two uterine horns. Embryos were isolated, transferred into a 24-well plate filled with PBS, and the head and the red organs (heart and liver) were removed. The rest of the embryo was placed into a 12-well plate filled with 2 ml ice-cold 0.25 % Trypsin/PBS (diluted from 2.5 % Trypsin, Gibco). The embryos were chopped into small pieces and incubated overnight at 4 °C. Then, the trypsin solution was discarded and the remaining Trypsin/tissue mixture was incubated for 30 min in a 37 °C water bath. Afterwards of medium (composition: DMEM/Glutamax, 10 % FCS, 1 % sodium pyruvate (100x), 1 % Pen Strep), was added, and the cell suspension was pipetted vigorously up and down to break up the digested tissue into a single cell suspension. After 1 min to allow sedimentation of the remaining tissue, the cell suspension was transferred into a new tube. This step was repeated and afterwards, the cell suspension was filtered through a 100 µm cell-strainer (Corning). Cells were plated and after 24 h, the medium was changed. Immortalization of MEFs was performed as described previously (Todaro and Green, 1963). Briefly, cells are split every three days and seeded with the same cell density. From passage three onwards, cells were seeded on at least two 10 cm culture dishes. After around 15 passages, cells started to regrow. When MEFs were immortalized, frozen back-ups were made.

Magnetic Activated Cell Sorting (MACS)

MACS was performed according to manufacturer's instructions (Miltenyi Biotec) For negative selection, suspended cells were incubated with biotinylated anti-CD45, anti-CD31, and anti-TER119 antibodies (Biolegend), followed by incubation with Streptavidin MicroBeads (Miltenyi Biotec). Samples were run through LD columns (Miltenyi Biotec) followed by three washes with MACS buffer (0.5% BSA, 2.5 mM EDTA in PBS). Unlabeled cells were collected and either cultured (referred to as SVF Lin- cells or further incubated with anti-CD54 (Biolegend) and anti-VAP1 (abcam) antibodies followed by Streptavidin MicroBeads. Unlabeled cells were collected using LS columns (Miltenyi Biotec). After three washes with MACS buffer, cells were eluted and used for downstream applications.

Flow cytometry and fluorescence-assisted cell sorting (FACS)

Mouse antibodies for flow cytometry were purchased from Biolegend, Thermo Fisher Scientific, Miltenyi Biotec, and BD Biosciences (Tab. S5).

Isolated SVF cells were stained with primary antibodies for 30 min on ice, washed, and stained with the secondary antibody for 15 min on ice. Hoechst 33258 (Thermo Fischer) or LIVE/DEAD™ Fixable Near-IR Dead Cell Stain Kit (Thermo Fischer) were used to exclude dead cells.

Data were acquired on a Sony ID700 spectral cytometer (BD Biosciences) or the Attune NxT Flow Cytometer (Thermo Fischer Scientific) and analyzed with the FlowJo software (Tree Star). To generate the UMAP, the SCA1$^+$ gate was down-sampled and samples from all experiments were concatenated into one file to be analyzed by a custom-made R script kindly provided by the group of Elvira Mass. FACS was performed on a BD FACSAria III cell sorter.

Immunocytochemistry

Cells were fixed with 4% paraformaldehyde (PFA, 16% wt/vol ag. Soln., methanol free, Alfa Aesa) for 10 min and subsequently washed with PBS before blocking with CT (0.5% Triton X-100 (Sigma-Aldrich), 5% ChemiBLOCKER (Merck Millipore) in 0.1 M NaP, pH 7.0) for 30 min at room temperature. Primary and secondary antibodies were diluted in CT and incubated for 60 min at room temperature. DAPI (4′,6-diamidino-2-phenylindole, dihydrochloride, 1:10,000, Invitrogen) was used as a DNA counterstain together with the secondary antibody. For staining of lipid droplets, cells were incubated with the lipophilic dye LD540 (1:10,000) (Spandl et al., 2009) for 15 min and washed again with PBS. All antibodies are in table S6.

SVF culture and *in vitro* assays

Cells were maintained in maintenance medium containing DMEM/F12 (1:1), supplemented with 1% GlutaMAX-I, 1% penicillin-streptomycin (all Life Technologies/Life Technologies), 10% FCS (Biochrom), 33 mM biotin (Sigma), and 17 mM D-pantothenate (Sigma) at 37°C with 5% CO_2 in a cell culture incubator.

For the adipogenesis assay, isolated APCs were seeded on CellCarrier Ultra 96- or 384- well plates. When cells reached confluency, adipogenesis was induced by switching to their respective induction cocktail: a) Full Induction (FI) containing 5 µg/ml insulin, 1 µM Dexamethasone, 100 µM IBMX, and 1 µM rosiglitazone (Sigma); b) Minimal Induction (MI) (Hilgendorf et al., 2019) containing 0.4 µg/ml insulin (Sigma), 0.1 µM Dexamethasone (Sigma), and 20 µM 3-isobutyl-1-methylxanthine (IBMX; Sigma); c) Insulin only condition containing 0.4 µg/ml insulin. TUG891 (Tocris, #4601) was added at a concentration of 100 µM.

The medium was exchanged to freshly prepared maintenance medium, containing 1 µg/ml insulin on day 3 and 5. Additionally, as a negative control, undifferentiated cells without induction medium were kept in maintenance medium.

To induce Hh signaling in APCs or MEF cells, APCs were starved for 12 h or 24 h, respectively. Cells were then stimulated with 1 µM Smoothend Agonist (SAG, Sigma) or H_2O (vehicle) for 24 h. Cells were either harvested for RNA isolation or fixed for immunocytochemistry.

Pulse Chase analysis of fatty acid incorporation

Pulse chase analysis using alkyne-labeled fatty acids followed the protocol described in (Wunderling et al., 2023)**.** Isolated APCs were seeded on 48- well plates. When cells reached confluency, adipogenesis was induced by switching to a full induction cocktail for three days and then switching to 1 µg/ml insulin for one more day. Subsequently, cells were fed with growth medium containing 50□µM of each alkyne-fatty acids: FA 11:0;Y (TCI Deutschland GmbH), FA 18:2;Y (multistep synthesis done by Dr. Christoph Thiele) and 13C6-FA 16:0;Y (multistep synthesis done by Dr. Christoph Thiele), for 1□h. After 1h media were removed, cells were washed once with medium and fresh medium was added for the indicated chase times. After the chase, media were removed, and cells were washed with PBS and processed for extraction and analysis.

Lipid extraction and click reaction

All solvents were HPLC grade or LC-MS grade purchased from VWR International GmbH (Darmstadt, Germany) and Merck KGaA (Darmstadt, Germany).

To each well, 500 µl of extraction mix (490 µl MeOH/$CHCl_3$ 5/1, 10 µl internal standard mix containing alkyne-labeled standard lipids (Wunderling et al., 2023) and a non-alkyne internal standard for TG (TG 50:1[D4]) as indicated above were added and the entire plate was sonicated for 1 min in a bath sonicator. The extract including the cell remnants were collected into 1.5 ml original Eppendorf tubes and centrifuged at 20000 g for 5 min to pellet protein. The supernatants were transferred into fresh tubes. After addition of 400 µl $CHCl_3$ and 600 µl 1% AcOH in water, samples were shaken for 30 sec and centrifuged for 5 min at 20000 g. The upper phase was removed, the lower phase transferred into a fresh tube and dried for 20 min at 45°C in a speed-vak. $CHCl_3$ (8 µl) was added and the tubes briefly vortexed. To each tube 40 µl Click mix were added (prepared by mixing 10 µl of 100 mM C175-7x in 50% MeOH (stored as aliquots at -80°C) with 200 µl 5 mM Cu(I)$AcCN_4BF_4$ in AcCN and 800 µl ethanol) followed by sonication for 5 min and incubation at 40°C for 16 h.

To samples clicked with C175-7x, 100 µl $CHCl_3$ per sample was added and multiplex samples pooled. To the pool, 600 µl water was added and pools briefly shaken and centrifuged for 2 min at 20000 g. The upper phase was removed and the lower phase dried in a speed-vak as above. Spray buffer (200 - 1000 µl) was added, the tubes sonicated for 5 min and the dissolved lipids analyzed by MS.

Mass spectrometry

The dissolved lipids were analyzed on a Thermo Q Exactive Plus spectrometer equipped with a standard heated electrospray ionization ion source using direct injection from a Hamilton syringe driven by a syringe pump under the control of the Tune instrument control software. Instrument parameters and data analysis procedure (Wunderling et al., 2023). Raw files were converted to .mzml files using MSconvert and analyzed using LipidXplorer for lipid species that incorporated the alkyne fatty acid.

Quantitative RT-PCR

To isolate mRNA, primary adipocytes and adipose tissues were lysed within a monophasic solution of phenol and guanidine isothiocyanate reagent (TRI Reagent®, Sigma-Aldrich #T9424) following silica-based RNA spin column enrichment and eluted with RNAse/DNAse free water. RNA concentrations were measured using a spectrophotometer (Nanodrop, xxx) and RNA were used for reverse transcription (High-Capacity cDNA Reverse Transcription Kit, Thermo Fisher #4368813). Abundance of genes of interest was quantified using the

SYBR Green-based quantification method (FastStart Universal SYBR Green Mastermix, Roche® Life Science #4913914001) and mRNA abundance was calculated using relative quantification methods (Pfaffl Method; Pfaffl et al, 2001).

Transcript levels of mRNAs were normalized to Glycerinaldehyd-3-phosphat-Dehydrogenase (*Gapdh*) and tata-box binding protein (*Tatabp*) expressions. Primer sequences are provided in table S7.

Histology

Histological analysis was performed as previously described (Sieckmann et al, 2022). Briefly, WAT was fixed and further processed using the automated Epredia Excelsior AS Tissue Processor (ThermoFisher Scientific). Tissues were dehydrated, cleared in a clearing agent and xylene (AppliChem) before incubating in molten paraffin wax (Labomedic). Tissues were cast into molds together with liquid paraffin and cooled to form a solid paraffin block with embedded tissue (Leica EG1150 H Paraffin Embedding Station and Leica EG1150 C Cold Plate). Paraffin-embedded WAT was sliced into 5-µm sections using a ThermoScientific HM 355S Automatic Microtome and mounted on Surgipath X-tra Microscope Slides (Leica Biosystems).

For histological analysis WAT sections were stained with Hematoxylin and Eosin (H&E) or Sirius Red and Elastika van Gieson (EvG) and using the Leica ST5020 Multistainer combined with Leica CV5030 Fully Automated Glass Coverslipper. Deparaffinization of paraffin-embedded WAT slices was performed and three subsequent steps in xylene before incubation in a graded alcohol series (100–70% ethanol) to rehydrate the tissue sections and ending with a final rinsing step in sterile distilled water (dH2O). Next, tissue slices were stained with Mayer′s hemalum solution (Sigma Aldrich). To counterstain with Eosin Y solution (1% in water, Roth), slides were immersed in eosin. For the Sirius Red and EvG staining slides were firstly incubated in Resorcinol-Fuchsin, following staining in haematoxylin and finally Picro-Sirius Red solution. Next, slices were washed in 30% acetic acid and shorty stained in Picric Fuchsine. After each respective staining slides were incubated in a graded alcohol series (70–100% ethanol) to dehydrate the tissue. Paraffin embedding, slicing, and staining were conducted by the histology facility at University Hospital Bonn.

Microscopy and image analyses

Confocal z-stacks were recorded with a confocal microscope at the Microscopy Core Facility of the Medical Faculty at the University of Bonn (Leica SP8) or an Olympus Fluoview FV1000 confocal microscope at the caesar institute (Bonn). For quantifying fluorescence signals, z-stacks were recorded from at least two random positions per experiment and analyzed using “CiliaQ” (Hansen et al., 2021). CiliaQ was developed to fully automatically quantify the ciliary intensity levels in the different channels. In all plots, the parameter revealing the average intensity of the 10% of cilia pixels with highest intensity is shown as ciliary intensity level. From all values, the background intensity level was subtracted.

Fluorescence images of adipogenesis assays were taken at the CellDiscoverer 7 widefield microscope (Zeiss) using automated image acquisition. Two or four images were acquired per well, each in a z-stack (step size 4 µm, 10× magnification). Depicted images are shown as a projection of the sharpest plane including the plane above and below. A maximum projection around the sharpest plane was generated using the ImageJ plugin ExtractSharpestPlane_JNH (https://doi.org/10.5281/zenodo.5646492) (Hansen et al., 2021). Adipogenesis was quantified using “AdipoQ” (Sieckmann et al., 2022). Briefly, custom preferences for AdipoQ Preparator and AdipoQ were used to identify and analyze adipocytes.

Bulk RNA-sequencing and analysis

Subpopulations were sorted as described above and immediately stored in Trizol. Total RNA was extracted using the miRNeasy Micro kit (Qiagen) according to manufacturer’s protocol. RNA was quantified and RNA integrity was determined using the HS RNA assay on a Tapestation 4200 system (Agilent). Smart-seq2 was used for the generation of non-strand-specific, full transcript sequencing libraries using standard reagents and procedures as previously described (Picelli et al., 2014). Briefly, 250 pg of total RNA was transferred to buffer containing 0.2% TritonX-100, protein-based RNase inhibitor, dNTPs, and oligo-dT oligonucleotides to prime the subsequent RT reaction on polyadenylated mRNA sequences. The SMART RT reaction was performed at 42°C for 90 min using commercial SuperScript II (Invitrogen) and a TSO. A preamplification PCR of 14 cycles was performed to generate double-stranded DNA from the cDNA template. At least 200 pg of amplified cDNA were used for tagmentation reaction and subsequent PCR amplification using the Nextera XT kit (Illumina) to construct sequencing libraries. Libraries were quantified using the Qubit HS dsDNA assay, and library fragment size distribution was determined using the D1000 assay on a Tapestation 4200 system (Agilent). Samples were pooled and clustered at 1.25 nM on a NovaSeq6000 system (Illumina) to generate ~10 M single-read (75bp) reads per sample using a NovaSeq6000 XP kit. Raw sequencing data were demultiplexed using bcl2fastq2 v2.20.

The RNA-seq 3’ data were processed with nf-core RNA-seq v1.4.2 (Ewels et al., 2020) pipeline using STAR (Dobin et al., 2013) for alignment and featureCounts for gene quantification (Liao et al., 2014). The library strandedness parameter was set to forward and the reference was set to GRCm38. Statistical analysis was performed in the R environment (R Core Team, 2019) with the Bioconductor R-package DESeq2 (Love et al., 2014). The Benjamini-Hochberg method was used to calculate multiple testing adjusted p-values. Only genes with at least 10 read counts in at least 2 samples and at least 20 read counts in total across all samples were considered for analysis. Data visualization, such as volcano plots, were generated upon VST transferred data (Anders and Huber, 2010) using R-packages ggplot2 (v3. 3.3; Wickham, 2016). GO term and pathway enrichment analysis for differently expressed genes (FDR < 0.05, Fisher test) was performed using the Bioconductor packages packages fgsea, goseq (Subramanian et al., 2005; Young et al., 2010), and clusterProfiler (Wu et al., 2021).

Single-cell RNA-sequencing – sample preparation

Sequencing primarily relied on the Seq-Well S^3 protocol (Hughes et al., 2020), using two arrays per sample. Seq-Well arrays were prepared as described before (Gierahn et al., 2017). Each array was loaded with approximately 110,000 barcoded mRNA capture beads (ChemGenes, Cat: MACOSKO-2011-10) and with 30,000 cells. The procedure was executed as previously detailed (Hughes et al., 2020). After cell loading, cells were lysed, mRNA captured, and cDNA synthesis was performed. For the whole transcriptome amplification, beads from each array were distributed in 18-24 PCR reactions containing approximately 3,000 beads per PCR reaction (95°C for 3 min, 4 cycles of 98°C for 20 s, 65°C for 45 s, 63°C for 30 s, 72 °C for 1 min, 16 cycles of 98°C for 20 s, 67°C for 45 s, 72°C for 3 min and final 72 °C for 5 min) using KAPA HiFi Hotstart Readymix PCR Kit (Kapa Biosystems, Cat: KK2602) and SMART PCR Primer (AAGCAGTGGTATCAACGCAGAGT). 6-8 PCR reactions were pooled and purified with AMPure XP SPRI Reagent (Beckman Coulter), first at 0.6x and then at a 1x volumetric ratio. For the library tagmentation and indexing, 200 pg of DNA from the purified WTA from each pool were tagmented with the Nextera XT DNA Library Preparation Kit for 8 min at 55 °C followed by a Tn5 transposase neutralization for 5 min at RT. Finally, Illumina indices were attached to the tagmented products (72°C for 3 min, 98°C for 30 s, 16 cycles of 95°C for 10 s, 55°C for 30 s, 72°C for 1 min and final 72°C for 5 min). Library products were purified using AMPure XP SPRI Reagent, first at 0.6x and then at a 1× volumetric ratio. Final library quality was assessed using a High Sensitivity D5000 assay on a Tapestation 4200 (Agilent) and quantified using the Qubit high-sensitivity dsDNA assay (Invitrogen). Seq-Well libraries were equimolarly pooled and clustered at 1,25 nM concentration with 10% PhiX on a NovaSeq6000 system using a S2 flow cell with 100 bp v.1.5 chemistry. Sequencing was performed paired-end using custom Drop-Seq Read 1 primer for 21 cycles, 8 cycles for the i7 index, and 61 cycles for Read 2. Single-cell data were demultiplexed using bcl2fastq2 (v2.20). Fastq files from Seq-Well were loaded into a snakemake-based data pre-processing pipeline (version 0.31, available at https://github.com/Hoohm/dropSeqPipe) that relies on the Drop-seq tools provided by the McCarroll lab (Macosko, Basu et al. 2015). STAR alignment within the pipeline was performed using the murine GENCODE reference genome and transcriptome mm10 release vM16 (Team 2014).

Single-cell RNA-sequencing – data analysis

The scRNA-seq data analysis was conducted using the Seurat analysis pipeline (version 4.1.1) unless otherwise specified. To address differences in sequencing depth, the downsampleBatches function from the scuttle package (version 1.0.4) was employed using default parameter settings. Cells expressing fewer than 100 or more than 1000 genes, as well as those with more than 20 percent mitochondrial genes, were removed. The individual sequencing samples were integrated using 2000 variable features. Using the first 30 dimensions, the Louvain algorithm detected 16 cell clusters which were annotated using known marker gene panels (see Fig. S4c). Clusters with less than 60 cells (10% percentile) were removed from the dataset.

To account for sample size differences due to varying sequencing depths, the *Bbs8*$^{-/-}$ dataset was down-sampled according to the *Bbs8*$^{+/+}$ reference by grouping cells into 10 bins based on their UMAP 1 coordinates. Finally, 353 cells per bin were randomly selected from the *Bbs8*$^{-/-}$ dataset. A differential abundance analysis of each APC and FPC subpopulation across genotypes was performed using a Fisher’s exact test with p-values corrected using the FDR method. Developmental trajectories within the APC and FPC subpopulations were calculated using the monocle3 package (version 1.0.0). After re-clustering, the graph structure from the *Bbs8*$^{+/+}$ and down-sampled *Bbs8*$^{-/-}$ datasets was learned using default parameters while disabling graph pruning. Pseudotimes were computed using the APC P1 subpopulation as the root.

Differences in the murine GSEA Hallmark-Hedgehog (Hh) signature across genotypes within the APC and FPC subpopulation were assessed using Seurat’s AddModuleScore function. First, the Hallmark genes were filtered for expressed genes before calculating cell-wise Hh-signature scores. Those scores were grouped per genotype and compared using a Wilcoxon’s test within the down-sampled subset. Further characterization of the FPC population involved an overrepresentation analysis (ORA) employing the C2 MsigDB data repository, using the top 50 up- and down-regulated genes between FPCs and all other cell populations, as described (Kwon et al., 2023). The 50 top and bottom genes were identified by ranking them according to Bonferroni corrected p-values calculated using Seurat’s FindMarkers function. The C2 MsigDB data set was filtered for entries with less than 300 members to focus on gene-sets of comparable size to our input data. Finally, the pathway overrepresentation (Tab. S4) was calculated using the clusterprofiler package (version 3.18.1) with a q-value cutoff of 5%.

CellChat (v 1.6.1) (Jin et al., 2021) was used to analyze possible cell-cell interactions in the data. To find all possible interactions, the 'computeCommunProb' command was used with 'type = "truncatedMean"' and 'trim = 0' arguments. The analysis was run separately on data from *Bbs8*$^{+/+}$ and *Bbs8*$^{-/-}$ mice and compared after merging with the 'mergeCellChat' command.

Interaction difference heatmaps were created using the ComplexHeatmap package. Complex heatmaps reveal patterns and correlations in multidimensional genomic data (Gu et al., 2016).

In search for vessel-associated APC cells, the Seurat object was subset to contain only the three APC populations with the Fibroblast cluster. The 'FindSubCluster' command was used with 'resolution = 0.3' argument to create 2 subclusters of the APC P2 cluster. 90.50%, 88.46%, 87.34% of the cells of interest ('APC P2_1') still cluster together with 3, 4, or 5 subclusters created, respectively. The marker list (Tab. S3) was generated using the 'FindAllMarkers' command with 'logfc.threshold = 0.1' and 'only.pos = T' arguments, from...

... the APC populations.

... the APC populations and fibroblasts.

... the APC populations, fibroblasts, endothelial cells, and pericytes.

Quantification, statistical analysis and reproducibility

Results are presented as mean ± SEM or mean ± SD as indicated. The lean time point for each mouse line was chosen based on the mean body weight with the most similar value and smallest standard deviation. All body weights were then normalized to this mean, respective for each genotype. In box plots, boxes represent interquartile range and median, and whiskers indicate the minimum and maximum values. Each mouse represents an independent biological sample. Prism 8.2.0 software was used to calculate P values using a two-sided Mann–Whitney test, two-sided unpaired t-test, Kruskal–Wallis test with Dunn’s post test, two-way ANOVA or Mantel–Cox log-rank test as indicated. Prism 8.2.0 software or the R programming language was used to generate graphical representations of quantitative data unless stated otherwise. Exact P values are indicated in the figures. Sample sizes (n) are indicated in the figure legends.

Data availability

Non-commercially available reagents or mouse lines can be made available under a material transfer agreement with the University Hospital Bonn. All data inquiries should be addressed to DW. Image datasets generated during and/or analyzed during the current study are available through figshare https://figshare.com/projects/BBSome-dependent_ciliary_Hedgehog_signaling_governs_cell_fate_in_the_white_adipose_tissue/193025 RNA-Sequencing data were deposited in GEO and are available upon request.

Code availability

This paper does not report original code. All codes used in this paper are available from the DW upon request.

Supplemental information

Supplementary tables S1-S7, Supplementary figures S1-S4.

References

Altun, I., Yan, X., and Ussar, S. (2022). Immune Cell Regulation of White Adipose Progenitor Cell Fate. Front. Endocrinol. (Lausanne) *13*, 859044.

Anders, S., and Huber, W. (2010). Differential expression analysis for sequence count data. Genome Biol. *11*, R106.

Blüher, M. (2019). Obesity: global epidemiology and pathogenesis. Nat. Rev. Endocrinol. *15*, 288-298.

Boutari, C., and Mantzoros, C.S. (2022). A 2022 update on the epidemiology of obesity and a call to action: as its twin COVID-19 pandemic appears to be receding, the obesity and dysmetabolism pandemic continues to rage on. Metabolism *133*, 155217.

Brewer, K.M., Brewer, K.K., Richardson, N.C., and Berbari, N.F. (2022). Neuronal cilia in energy homeostasis. Front. Cell Dev. Biol. *10*, 1082141.

Burl, R.B., Ramseyer, V.D., Rondini, E.A., Pique-Regi, R., Lee, Y.H., and Granneman, J.G. (2018). Deconstructing Adipogenesis Induced by beta3-Adrenergic Receptor Activation with Single-Cell Expression Profiling. Cell Metab. *28*, 300-309 e304.

Cho, D.S., Lee, B., and Doles, J.D. (2019). Refining the adipose progenitor cell landscape in healthy and obese visceral adipose tissue using single-cell gene expression profiling. Life Sci. Alliance *2*.

Chouchani, E.T., and Kajimura, S. (2019). Metabolic adaptation and maladaptation in adipose tissue. Nat. Metab. *1*, 189-200.

Das, S.K., Roberts, S.B., Kehayias, J.J., Wang, J., Hsu, L.K., Shikora, S.A., Saltzman, E., and McCrory, M.A. (2003). Body composition assessment in extreme obesity and after massive weight loss induced by gastric bypass surgery. Am. J. Physiol. Endocrinol. Metab. *284*, E1080-1088.

DeMars, K.M., Ross, M.R., Starr, A., and McIntyre, J.C. (2023). Neuronal primary cilia integrate peripheral signals with metabolic drives. Front. Physiol. *14*, 1150232.

Dobin, A., Davis, C.A., Schlesinger, F., Drenkow, J., Zaleski, C., Jha, S., Batut, P., Chaisson, M., and Gingeras, T.R. (2013). STAR: ultrafast universal RNA-seq aligner. Bioinformatics *29*, 15-21.

Engle, S.E., Bansal, R., Antonellis, P.J., and Berbari, N.F. (2021). Cilia signaling and obesity. Semin. Cell Dev. Biol. *110*, 43-50.

Ewels, P.A., Peltzer, A., Fillinger, S., Patel, H., Alneberg, J., Wilm, A., Garcia, M.U., Di Tommaso, P., and Nahnsen, S. (2020). The nf-core framework for community-curated bioinformatics pipelines. Nat. Biotechnol. *38*, 276-278.

Ewerling, A., Maissl, V., Wickstead, B., and May-Simera, H.L. (2023). Neofunctionalization of ciliary BBS proteins to nuclear roles is likely a frequent innovation across eukaryotes. iScience *26*, 106410.

Ferrero, R., Rainer, P., and Deplancke, B. (2020). Toward a Consensus View of Mammalian Adipocyte Stem and Progenitor Cell Heterogeneity. Trends Cell Biol. *30*, 937-950.

Forsythe, E., and Beales, P.L. (2013). Bardet-Biedl syndrome. Eur. J. Hum. Genet. *21*, 8-13.

Gascue, C., Tan, P.L., Cardenas-Rodriguez, M., Libisch, G., Fernandez-Calero, T., Liu, Y.P., Astrada, S., Robello, C., Naya, H., Katsanis, N.*, et al.* (2012). Direct role of Bardet-Biedl syndrome proteins in transcriptional regulation. J. Cell Sci. *125*, 362-375.

Gierahn, T.M., Wadsworth, M.H., 2nd, Hughes, T.K., Bryson, B.D., Butler, A., Satija, R., Fortune, S., Love, J.C., and Shalek, A.K. (2017). Seq-Well: portable, low-cost RNA sequencing of single cells at high throughput. Nat. Methods *14*, 395-398.

Gopalakrishnan, J., Feistel, K., Friedrich, B.M., Grapin-Botton, A., Jurisch-Yaksi, N., Mass, E., Mick, D.U., Muller, R.U., May-Simera, H., Schermer, B.*, et al.* (2023). Emerging principles of primary cilia dynamics in controlling tissue organization and function. EMBO J. *42*, e113891.

Gupta, R.K., Mepani, R.J., Kleiner, S., Lo, J.C., Khandekar, M.J., Cohen, P., Frontini, A., Bhowmick, D.C., Ye, L., Cinti, S.*, et al.* (2012). Zfp423 expression identifies committed preadipocytes and localizes to adipose endothelial and perivascular cells. Cell Metab. *15*, 230-239.

Hansen, J.N., Rassmann, S., Stüven, B., Jurisch-Yaksi, N., and Wachten, D. (2021). CiliaQ: a simple, open-source software for automated quantification of ciliary morphology and fluorescence in 2D, 3D, and 4D images. Eur. Phys. J. E. Soft Matter *44*, 18.

Hasegawa, Y. (2022). New perspectives on obesity-induced adipose tissue fibrosis and related clinical manifestations. Endocr. J. *69*, 739-748.

Hepler, C., Shan, B., Zhang, Q., Henry, G.H., Shao, M., Vishvanath, L., Ghaben, A.L., Mobley, A.B., Strand, D., Hon, G.C.*, et al.* (2018). Identification of functionally distinct fibro-inflammatory and adipogenic stromal subpopulations in visceral adipose tissue of adult mice. eLife *7*.

Hey, C.A.B., Larsen, L.J., Tumer, Z., Brondum-Nielsen, K., Gronskov, K., Hjortshoj, T.D., and Moller, L.B. (2021). BBS Proteins Affect Ciliogenesis and Are Essential for Hedgehog Signaling, but Not for Formation of iPSC-Derived RPE-65 Expressing RPE-Like Cells. Int. J. Mol. Sci. *22*.

Hildreth, A.D., Ma, F., Wong, Y.Y., Sun, R., Pellegrini, M., and O'Sullivan, T.E. (2021). Single-cell sequencing of human white adipose tissue identifies new cell states in health and obesity. Nat. Immunol. *22*, 639-653.

Hilgendorf, K.I. (2021). Primary Cilia Are Critical Regulators of White Adipose Tissue Expansion. Front Physiol *12*, 769367.

Hilgendorf, K.I., Johnson, C.T., Mezger, A., Rice, S.L., Norris, A.M., Demeter, J., Greenleaf, W.J., Reiter, J.F., Kopinke, D., and Jackson, P.K. (2019). Omega-3 Fatty Acids Activate Ciliary FFAR4 to Control Adipogenesis. Cell *179*, 1289-1305 e1221.

Horwitz, A., and Birk, R. (2021). BBS4 Is Essential for Nuclear Transport of Transcription Factors Mediating Neuronal ER Stress Response. Mol. Neurobiol. *58*, 78-91.

Horwitz, A., and Birk, R. (2023). Adipose Tissue Hyperplasia and Hypertrophy in Common and Syndromic Obesity-The Case of BBS Obesity. Nutrients *15*.

Hughes, T.K., Wadsworth, M.H., 2nd, Gierahn, T.M., Do, T., Weiss, D., Andrade, P.R., Ma, F., de Andrade Silva, B.J., Shao, S., Tsoi, L.C.*, et al.* (2020). Second-Strand Synthesis-Based Massively Parallel scRNA-Seq Reveals Cellular States and Molecular Features of Human Inflammatory Skin Pathologies. Immunity *53*, 878-894 e877.

Jääskelainen, I., Petäisto, T., Mirzarazi Dahagi, E., Mahmoodi, M., Pihlajaniemi, T., Kaartinen, M.T., and Heljasvaara, R. (2023). Collagens Regulating Adipose Tissue Formation and Functions. Biomedicines *11*.

Jin, S., Guerrero-Juarez, C.F., Zhang, L., Chang, I., Ramos, R., Kuan, C.H., Myung, P., Plikus, M.V., and Nie, Q. (2021). Inference and analysis of cell-cell communication using CellChat. Nat. Commun. *12*, 1088.

Kopinke, D., Norris, A.M., and Mukhopadhyay, S. (2021). Developmental and regenerative paradigms of cilia regulated hedgehog signaling. Semin. Cell Dev. Biol. *110*, 89-103.

Kopinke, D., Roberson, E.C., and Reiter, J.F. (2017). Ciliary Hedgehog Signaling Restricts Injury-Induced Adipogenesis. Cell *170*, 340-351 e312.

Krueger, K.C., Costa, M.J., Du, H., and Feldman, B.J. (2014). Characterization of Cre recombinase activity for in vivo targeting of adipocyte precursor cells. Stem Cell Rep. *3*, 1147-1158.

Liao, Y., Smyth, G.K., and Shi, W. (2014). featureCounts: an efficient general purpose program for assigning sequence reads to genomic features. Bioinformatics *30*, 923-930.

Love, M.I., Huber, W., and Anders, S. (2014). Moderated estimation of fold change and dispersion for RNA-seq data with DESeq2. Genome Biol. *15*, 550.

Marcelin, G., Ferreira, A., Liu, Y., Atlan, M., Aron-Wisnewsky, J., Pelloux, V., Botbol, Y., Ambrosini, M., Fradet, M., Rouault, C.*, et al.* (2017). A PDGFRalpha-Mediated Switch toward CD9(high) Adipocyte Progenitors Controls Obesity-Induced Adipose Tissue Fibrosis. Cell Metab. *25*, 673-685.

Marion, V., Mockel, A., De Melo, C., Obringer, C., Claussmann, A., Simon, A., Messaddeq, N., Durand, M., Dupuis, L., Loeffler, J.P.*, et al.* (2012). BBS-induced ciliary defect enhances adipogenesis, causing paradoxical higher-insulin sensitivity, glucose usage, and decreased inflammatory response. Cell Metab. *16*, 363-377.

Massier, L., Jalkanen, J., Elmastas, M., Zhong, J., Wang, T., Nono Nankam, P.A., Frendo-Cumbo, S., Backdahl, J., Subramanian, N., Sekine, T.*, et al.* (2023). An integrated single cell and spatial transcriptomic map of human white adipose tissue. Nat. Commun. *14*, 1438.

Merrick, D., Sakers, A., Irgebay, Z., Okada, C., Calvert, C., Morley, M.P., Percec, I., and Seale, P. (2019). Identification of a mesenchymal progenitor cell hierarchy in adipose tissue. Science *364*.

Mill, P., Christensen, S.T., and Pedersen, L.B. (2023). Primary cilia as dynamic and diverse signalling hubs in development and disease. Nat. Rev. Genet.

Nachury, M.V. (2018). The molecular machines that traffic signaling receptors into and out of cilia. Curr. Opin. Cell Biol. *51*, 124-131.

Nahmgoong, H., Jeon, Y.G., Park, E.S., Choi, Y.H., Han, S.M., Park, J., Ji, Y., Sohn, J.H., Han, J.S., Kim, Y.Y.*, et al.* (2022). Distinct properties of adipose stem cell subpopulations determine fat depot-specific characteristics. Cell Metab. *34*, 458-472 e456.

Nguyen, H.P., Lin, F., Yi, D., Xie, Y., Dinh, J., Xue, P., and Sul, H.S. (2021). Aging-dependent regulatory cells emerge in subcutaneous fat to inhibit adipogenesis. Dev. Cell *56*, 1437-1451 e1433.

Norris, A.M., Appu, A.B., Johnson, C.D., Zhou, L.Y., McKellar, D.W., Renault, M.A., Hammers, D., Cosgrove, B.D., and Kopinke, D. (2023). Hedgehog signaling via its ligand DHH acts as cell fate determinant during skeletal muscle regeneration. Nat. Commun. *14*, 3766.

Park, K., and Leroux, M.R. (2022). Composition, organization and mechanisms of the transition zone, a gate for the cilium. EMBO Rep. *23*, e55420.

Picelli, S., Faridani, O.R., Bjorklund, A.K., Winberg, G., Sagasser, S., and Sandberg, R. (2014). Full-length RNA-seq from single cells using Smart-seq2. Nat. Protoc. *9*, 171-181.

Picon-Galindo, E., Latz, E., and Wachten, D. (2022). Primary cilia and their effects on immune cell functions and metabolism: a model. Trends Immunol. *43*, 366-378.

Rahmouni, K., Fath, M.A., Seo, S., Thedens, D.R., Berry, C.J., Weiss, R., Nishimura, D.Y., and Sheffield, V.C. (2008). Leptin resistance contributes to obesity and hypertension in mouse models of Bardet-Biedl syndrome. J. Clin. Invest. *118*, 1458-1467.

Rodriguez, C.I., Buchholz, F., Galloway, J., Sequerra, R., Kasper, J., Ayala, R., Stewart, A.F., and Dymecki, S.M. (2000). High-efficiency deleter mice show that FLPe is an alternative to Cre-loxP. Nat. Genet. *25*, 139-140.

Rosen, E.D., and MacDougald, O.A. (2006). Adipocyte differentiation from the inside out. Nat. Rev. Mol. Cell Biol. *7*, 885-896.

Sarvari, A.K., Van Hauwaert, E.L., Markussen, L.K., Gammelmark, E., Marcher, A.B., Ebbesen, M.F., Nielsen, R., Brewer, J.R., Madsen, J.G.S., and Mandrup, S. (2021). Plasticity of Epididymal Adipose Tissue in Response to Diet-Induced Obesity at Single-Nucleus Resolution. Cell Metab. *33*, 437-453 e435.

Scamfer, S.R., Lee, M.D., and Hilgendorf, K.I. (2022). Ciliary control of adipocyte progenitor cell fate regulates energy storage. Front. Cell Dev. Biol. *10*, 1083372.

Schwalie, P.C., Dong, H., Zachara, M., Russeil, J., Alpern, D., Akchiche, N., Caprara, C., Sun, W., Schlaudraff, K.U., Soldati, G.*, et al.* (2018). A stromal cell population that inhibits adipogenesis in mammalian fat depots. Nature *559*, 103-108.

Scott, C.A., Marsden, A.N., Rebagliati, M.R., Zhang, Q., Chamling, X., Searby, C.C., Baye, L.M., Sheffield, V.C., and Slusarski, D.C. (2017). Nuclear/cytoplasmic transport defects in BBS6 underlie congenital heart disease through perturbation of a chromatin remodeling protein. PLoS Genet. *13*, e1006936.

Seo, S., Zhang, Q., Bugge, K., Breslow, D.K., Searby, C.C., Nachury, M.V., and Sheffield, V.C. (2011). A novel protein LZTFL1 regulates ciliary trafficking of the BBSome and Smoothened. PLoS Genet. *7*, e1002358.

Sieckmann, K., Winnerling, N., Huebecker, M., Leyendecker, P., Juliana Silva Ribeiro, D., Gnad, T., Pfeifer, A., Wachten, D., and Hansen, J.N. (2022). AdipoQ-a simple, open-source software to quantify adipocyte morphology and function in tissues and in vitro. Mol. Biol. Cell *33*, br22.

Spandl, J., White, D.J., Peychl, J., and Thiele, C. (2009). Live cell multicolor imaging of lipid droplets with a new dye, LD540. Traffic *10*, 1579-1584.

Subramanian, A., Tamayo, P., Mootha, V.K., Mukherjee, S., Ebert, B.L., Gillette, M.A., Paulovich, A., Pomeroy, S.L., Golub, T.R., Lander, E.S., *et al.* (2005). Gene set enrichment analysis: a knowledge-based approach for interpreting genome-wide expression profiles. Proc. Natl. Acad. Sci. USA *102*, 15545-15550.

Sun, K., Li, X., and Scherer, P.E. (2023). Extracellular Matrix (ECM) and Fibrosis in Adipose Tissue: Overview and Perspectives. Compr. Physiol. *13*, 4387-4407.

Tadenev, A.L., Kulaga, H.M., May-Simera, H.L., Kelley, M.W., Katsanis, N., and Reed, R.R. (2011). Loss of Bardet-Biedl syndrome protein-8 (BBS8) perturbs olfactory function, protein localization, and axon targeting. Proc Natl Acad Sci U S A *108*, 10320-10325.

Tang, W., Zeve, D., Suh, J.M., Bosnakovski, D., Kyba, M., Hammer, R.E., Tallquist, M.D., and Graff, J.M. (2008). White fat progenitor cells reside in the adipose vasculature. Science *322*, 583-586.

Todaro, G.J., and Green, H. (1963). Quantitative studies of the growth of mouse embryo cells in culture and their development into established lines. J. Cell Biol. *17*, 299-313.

Toyoda, S., Shin, J., Fukuhara, A., Otsuki, M., and Shimomura, I. (2022). Transforming growth factor beta1 signaling links extracellular matrix remodeling to intracellular lipogenesis upon physiological feeding events. J. Biol. Chem. *298*, 101748.

Vegiopoulos, A., Rohm, M., and Herzig, S. (2017). Adipose tissue: between the extremes. EMBO J. *36*, 1999-2017.

Vijay, J., Gauthier, M.F., Biswell, R.L., Louiselle, D.A., Johnston, J.J., Cheung, W.A., Belden, B., Pramatarova, A., Biertho, L., Gibson, M., *et al.* (2020). Single-cell analysis of human adipose tissue identifies depot and disease specific cell types. Nat. Metab. *2*, 97-109.

Wachten, D., and Mick, D.U. (2021). Signal transduction in primary cilia - analyzing and manipulating GPCR and second messenger signaling. Pharmacol. Ther. *224*, 107836.

Watt, F.M., and Huck, W.T. (2013). Role of the extracellular matrix in regulating stem cell fate. Nat. Rev. Mol. Cell Biol. *14*, 467-473.

White, U. (2023). Adipose tissue expansion in obesity, health, and disease. Front. Cell Dev. Biol. *11*, 1188844.

Wingfield, J.L., Lechtreck, K.F., and Lorentzen, E. (2018). Trafficking of ciliary membrane proteins by the intraflagellar transport/BBSome machinery. Essays Biochem. *62*, 753-763.

Wu, T., Hu, E., Xu, S., Chen, M., Guo, P., Dai, Z., Feng, T., Zhou, L., Tang, W., Zhan, L., *et al.* (2021). clusterProfiler 4.0: A universal enrichment tool for interpreting omics data. Innovation (Camb) *2*, 100141.

Wunderling, K., Zurkovic, J., Zink, F., Kuerschner, L., and Thiele, C. (2023). Triglyceride cycling enables modification of stored fatty acids. Nat. Metab. *5*, 699-709.

Yanardag, S., and Pugacheva, E.N. (2021). Primary Cilium Is Involved in Stem Cell Differentiation and Renewal through the Regulation of Multiple Signaling Pathways. Cells *10*.

Ye, J., Gao, C., Liang, Y., Hou, Z., Shi, Y., and Wang, Y. (2023). Characteristic and fate determination of adipose precursors during adipose tissue remodeling. Cell. Regen. *12*, 13.

Young, M.D., Wakefield, M.J., Smyth, G.K., and Oshlack, A. (2010). Gene ontology analysis for RNA-seq: accounting for selection bias. Genome Biol. *11*, R14.

Zhang, Q., Nishimura, D., Vogel, T., Shao, J., Swiderski, R., Yin, T., Searby, C., Carter, C.S., Kim, G., Bugge, K., *et al.* (2013). BBS7 is required for BBSome formation and its absence in mice results in Bardet-Biedl syndrome phenotypes and selective abnormalities in membrane protein trafficking. J. Cell Sci. *126*, 2372-2380.

Acknowledgement

We thank Jens-Henning Krause, Maximilian Rothe, and Romina Kaiser for technical support. We thank L. Sorokin for critically reading the manuscript and T. Schulz for providing the PDGFRα-Cre mice. We also thank the following Core Facilities of the Medical Faculty at the University of Bonn: Dr. Andreas Buness and Dr. Anshupa Sahu from the Core Facility Bioinformatics for help with data analysis; the Microscopy Core Facility for providing help, services, and devices funded by the Deutsche Forschungsgemeinschaft (DFG, German Research Foundation) – project numbers 388168919, 388158066, and 266686698; the Flow Cytometry Core Facility for providing help, services, and devices funded by the Deutsche Forschungsgemeinschaft (DFG, German Research Foundation) – project numbers 216372545 and 471514137; the Histology Platform of the ImmunoSensation^2 Cluster of Excellence, SFB 1454 – Project-ID 432325352 (to DW, EM, MB), TRR333/1 – Project-ID 450149205 (to DW), under Germany's Excellence Strategy – EXC2151 – Project-ID 390873048 (to DW, EM), FOR5547 – Project-ID 503306912 (to DW, EM, HLMS), WA 3382/8-1 – Project-ID 513767027, the Else Kröner Fresenius Foundation (2021.EKFSE.53) as well as intramural funding from the University of Bonn. EM is supported by the European Research Council (ERC) under the European Union's Horizon 2020 research and innovation program (Grant Agreement No. 851257). KS was supported with a PhD fellowship from the Studienstiftung des Deutschen Volkes and DJSR was supported by a Postdoc fellowship from the Walter-Benjamin Program of the Deutsche Forschungsgemeinschaft (DFG, German Research Foundation). HLMS was funded by the Alexander von Humboldt Foundation (Sofja Kovalevskaja Award). CRA is supported by the European Research Council (ERC) - ERC-consolidator grant (ref. 864875) and by a DFG grant SFB1366 - Project-ID - 394046768.

Author contributions

KS, NW, DW conceived and designed the analysis, KS, NW, RK, DJSR, CK, NB, JS, CT collected the data, KS, NW, DJSR, LMS, GS, LB, JSS, MB, COS, KT, JS, CT performed the analysis, HLMS, MB, contributed tools, KS, EM, CRA, DW wrote the paper.

Competing interest statement

The authors declare no conflicting financial interest.

Figure legends

Fig. 1 Primary cilia regulate the adipogenic potential of adipocytes precursors subpopulations (APCs). a, Schematics of the three adipocyte precursor subpopulations (APC) and their respective function and developmental hierarchy. **b,** Dimension reduction analysis from flow cytometry data based on the expression of the surface markers CD26, CD55, CD54, and CD142 revealed three distinct APC subpopulations (P1, P2, P3) in the Uniform Manifold Approximation and Projection (UMAP) two-dimensional map. **c,** Fluorescence intensities of the different markers in the UMAP, highlighting the contribution of each marker to the respective clusters. **d,** Frequency distribution of P1-P3 from the total APC pool (Sca1$^+$ cells). Each data point represents one animal. **e,** Fluorescence confocal images of FACS-sorted P1, P2, and P3 cells, labeled against ARL13B (yellow, cilia) and with DAPI (blue, DNA). **f,** Quantification of the ciliation rate from the sorted APCs subpopulations. Each data point represents one image from n = 3 wild-type mice in total. **g,** Fluorescence confocal images of FACS-sorted P1 and P2 cells, labeled against FABP4 (magenta, commitment adipogenic lineage), ARL13B, and with DAPI. **h,** Quantification of FABP4-positive cells. Each data point represents one image from n = 3 wild-type mice in total. **i,** Fluorescence images of *in-vitro* differentiated P1 and P2 APCs. Cells were differentiated for 8 days under full induction (FI) or minimal induction (MI) with or without addition of TUG-891 (100 µM). Cells were stained with LD540 (green, lipid droplets) and DAPI. **j,** Adipogenic potential of P1 and P2 APCs was quantified by calculating the ratio of the lipid droplet area and the area of nuclei. Each data point represents one image from n = 3 wild-type mice in total. All data are represented as mean ± SD, p-values were determined using an unpaired Student's t-test. Scale bars are indicated.

Fig. 2 Loss of BBS8 in APCs results in obesity. a, Relative body weight gain of chow diet-fed *Bbs8*$^{+/+}$ and *Bbs8*$^{-/-}$ mice. Weights were normalized to the mean body weight of their respective genotypes at the lean time point (10 weeks). Data are shown mean ± SEM, p-values were determined using a Two-way ANOVA with repeated measurements (mixed models). Post-hoc p-value correction for multiple testing was performed using Bonferroni adjustment (n = 14). **b,** Tissue weights of adipose tissues and liver at 15-18 weeks. Data are shown as mean ± SD, p-values has been determined using an unpaired Student's t-test determined, each data point represents one animal. **c,** Relative adipocyte cell size at the lean (7 weeks) and obese (15-18 weeks) state. Cell size was normalized to the lean timepoint of the respective genotype. Data are shown as mean ± SD, p-values have been determined using an unpaired Student's t-test, each data point represents one animal. **d,** Representative images of hematoxylin-eosin (HE)-stained gonadal WAT (gWAT) at 15-18 weeks. Scale bar = 100 µm. **e-f,** Adipocyte size distribution quantified using images as shown in (d) at 7 weeks

(e) and 15-18 weeks **(f)**. Data are shown as mean ± SD, p-values has been determined using an unpaired multiple Mann-Whitney tests with Bonferroni correction (n = 6-9 animals per genotype with >100 cells each). **g,** Adipose tissue weights at 17-21 weeks. Data are shown as mean ± SD, p-values has been determined using an unpaired Student's t-test determined, each data point represents one animal. **h,** Ratio of adipose tissue *vs.* body weight for each respective animal from the different mouse lines. Data are shown as mean ± SD, p-values has been determined using an unpaired Student's t-test determined, each data point represents one animal.

Fig. 3 Loss of Bbs8 induces a fibrogenic switch and ECM remodeling. a, Frequency distribution of P1-P3 from the total APC pool from *Bbs8*$^{+/+}$ (n = 26) and *Bbs8*$^{-/-}$ mice (n = 20). P-values were determined using unpaired Student's t-test. **b,** Principal Component Analysis (PCA) of the bulk RNA-seq data of FACS-sorted P1, P2, and P3 APCs from *Bbs8*$^{+/+}$ and *Bbs8*$^{-/-}$ mice based on the 500 most variable genes. **c,** Expression level of published P1, P2, and P3 markers. Data are shown as mean ± SD. **d,** Volcano plots depicting the DEGs for P1 APCs. **e,** Over-representation analysis (ORA) of DEGs, highlighting the top 10 biological processes from gene ontology analysis in *Bbs8*$^{-/-}$ P1 APCs compared to *Bbs8*$^{+/+}$ P1 APCs. **f,** Expression level of selected fibrosis marker genes in *Bbs8*$^{+/+}$ and *Bbs8*$^{-/-}$ P1 APCs. Data are shown as mean ± SD. **g,** Relative mRNA expression of fibrosis marker of sorted P1 APCs from *Bbs8*$^{+/+}$ and *Bbs8*$^{-/-}$ mice assessed by qRT-PCR. mRNA expression was normalized to *Bbs8*$^{+/+}$. **h,** Gating strategy demonstrated on concatenated *Bbs8*$^{+/+}$ and *Bbs8*$^{-/-}$ files (left). Quantification of CD9^{high} cell surface expression on PDGFRα^{+} cells from *Bbs8*$^{+/+}$ and *Bbs8*$^{-/-}$ mice (right). Data are shown as mean ± SD, p-values have been determined using an unpaired Student's t-test (n = 3). **i,** Sirius Red and Elastin-van-Giesson staining of gWAT from lean *Bbs8*$^{+/+}$ and *Bbs8*$^{-/-}$ mice. Scale bar = 50 µm. **j,** Fluorescence images of FACS-sorted, *in-vitro* differentiated gWAT PDGFRa^{+}/CD9^{hi} *Bbs8*$^{-/-}$ cells. Cells were differentiated for 8 days using the minimal induction (MI) with and without TUG-891 (100 µM). Cells were stained with LD540 (lipid droplets) and DAPI. Scale bars is indicated. **k,** The adipogenic potential of PDGFRα^{+}/CD9^{high} *Bbs8*$^{-/-}$ cells was quantified. Each data point represents the mean of all images from n = 3 mice in total. All data are represented as mean ± SD, p-values were determined using an unpaired Student's t-test. **l,** Uptake of triacyl glycerides (TAG) with respect to phosphatidylcholine (PC) after 4 days of *in-vitro* differentiation P1 cells from *Bbs8*$^{+/+}$ and *Bbs8*$^{-/-}$ mice with full induction cocktail. Data is normalized to *Bbs8*$^{+/+}$. Each data point represents one mouse from n = 4 mice in total. All data are represented as mean ± SD, p-values were determined using an unpaired Student's t-test.

Fig. 4 Loss of BBS8 drives P1 cells into fibrogenic cells. a, UMAP plot analysis from scRNA-seq data on iWAT SVF from lean *Bbs8*$^{+/+}$ and *Bbs8*$^{-/-}$ mice shows several distinct cell clusters. **b,** Expression levels of published P1, P2, and P3 markers in APCs and fibrogenic precursor cells (FPC). **c,** UMAP plot of the P1-P3 APCs and FPC cluster in *Bbs8*$^{+/+}$ and *Bbs8*$^{-/-}$ mice. **d,** P1, P2, and P3 marker expression overlayed over the subsetted UMAP displayed in (c). **e.** Differential abundance analysis of down-sampled clusters in *Bbs8*$^{-/-}$ compared to *Bbs8*$^{+/+}$ mice, the color-code shows FDR-corrected p-values. **f,** *In-silico* pseudo-time analysis of the P1-P3 APCs and FPCs along differentiation trajectories using Monocle3. **g,** Circos plots depicting the interaction strength between endothelial cells, pericytes, APC P1-P3, and FPCs as determined via the CellChat pipeline. **h,** Heat map depicting the differential interaction strength of the different APC subpopulations, endothelial cells, pericytes, and FPC. The interaction strength is color-coded. **i,** Dot plot showing the expression of collagen and laminin genes in the different APC subpopulations, in endothelial cells, pericytes, and FPC. The average gene expression is color-coded, the percentage of expression is expressed by the size of the dot. **j,** Dot plot of the collagen and laminin pathways in *Bbs8*$^{+/+}$ and *Bbs8*$^{-/-}$ cells. The p-value is color-coded, the probability of expression is expressed by the size of the dot.

Fig. 5 Loss of BBS8 results in ectopic Hedgehog (Hh) signaling and diminishes the Hh-dependent signaling response. a, Average expression of the hedgehog signature for the GSEA gene set HALLMARK_HEDGEHOG_SIGNALING calculated as the module score for all *Bbs8*$^{+/+}$ and down-sampled *Bbs8*$^{-/-}$ APCs, derived from scRNA-seq data. Violin plots represent the expression distribution of all cells. p-value was determined by Wilcoxon test. **b,** Fluorescence confocal images of lineage-depleted iWAT SVF from *Bbs8*$^{+/+}$ and *Bbs8*$^{-/-}$ mice, labeled against Smoothened (green, SMO) ARL13B (red, cilia), γ-Tubulin (magenta, basal body), and with DAPI (blue). Cells were treated with H_2O (control) or 1 µM SAG for 24 h. Scale bars are indicated. In all images, the green channel (SMO) was shifted by 10 px to the bottom for better visualizing SMO accumulation in cilia. **c,** Quantification of the ciliary SMO localization. The average intensity of the 10% highest SMO pixels in the ciliary (ARL13B) mask is depicted. Each data point represents >10 cilia from one animal (n = 9 mice in total). All data are shown as mean ± SD, p-values have been determined using a Two-way ANOVA with repeated measurements (mixed models). **d,** Relative mRNA expression of *Gli1* and *Ptch1* in linage-depleted SVF from *Bbs8*$^{+/+}$ and *Bbs8*$^{-/-}$ mice assessed by qRT-PCR. The expression was normalized to *Bbs8*$^{+/+}$ expression values. Each data point represents one animal. **e,** Relative mRNA expression of *Gli1* and *Ptch1* in linage-depleted SVF from *Bbs8*$^{+/+}$ and *Bbs8*$^{-/-}$ mice treated with SAG (1 µM) for 24 h. Expression was normalized to *Bbs8*$^{+/+}$ expression values. Each data point represents one animal (n > 7 mice). All data are shown as mean ± SD, p-values have been determined using an unpaired Student's t-test. **f**, Quantification of the ciliary SMO localization in mouse embryonic fibroblasts (MEF) cells. The colocalization of SMO pixels in the ciliary (ARL13B) mask is depicted. Each data point represents >10 cilia from one animal (n = 3 mice). **g,** Relative mRNA expression of *Ptch1* in MEF cells from *Bbs8*$^{+/+}$ and *Bbs8*$^{-/-}$ mice assessed by qRT-PCR. The expression was normalized to *Bbs8*$^{+/+}$ expression values. Each data point represents one animal. All data are shown as mean ± SD, p-values have been determined using a Two-way ANOVA. **h,** Relative mRNA expression of *Ptch1* in MEF cells from *Bbs8*$^{+/+}$ and *Bbs8*$^{-/-}$ mice treated with SAG (1 µM) for 24 h. Expression was normalized to *Bbs8*$^{+/+}$ expression values. Each data point represents one animal (n = 3 mice). All data are shown as mean ± SD, p-values have been determined using an unpaired Student's t-test.

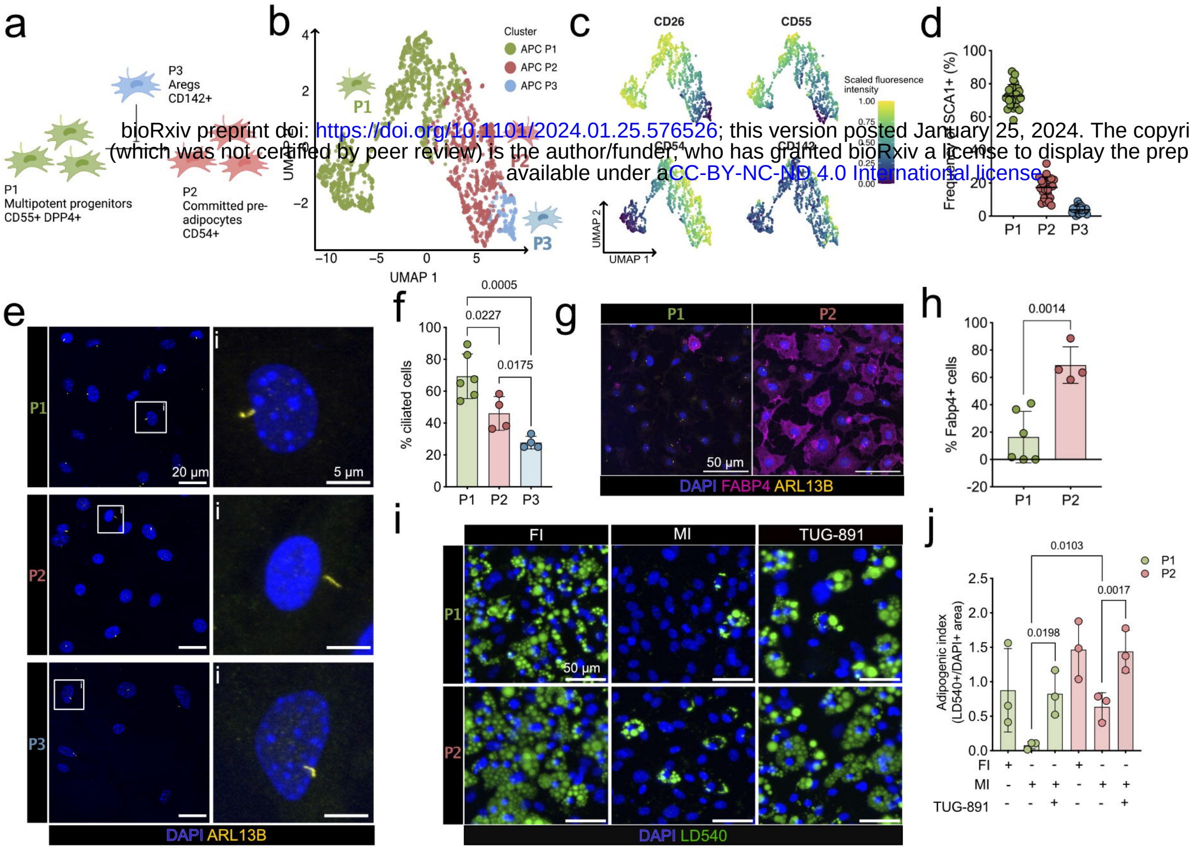
a
P3
Aregs
CD142+
P1
Multipotent progenitors
CD55+ DPP4+
P2
Committed pre-adipocytes
CD54+
b
Cluster
APC P1
APC P2
APC P3
P1
P2
P3
UMAP 2
UMAP 1
4
2
−2
−10
−5
0
5
c
CD26
CD55
CD54
CD142
Scaled fluoresence intensity
1.00
0.75
0.50
0.25
0.00
UMAP 2
UMAP 1
d
Frequency of SCA1+ (%)
100
80
60
40
20
0
P1
P2
P3
e
P1
P2
P3
i
20 µm
5 µm
DAPI ARL13B
f
% ciliated cells
0.0005
0.0227
0.0175
100
80
60
40
20
0
P1
P2
P3
g
P1
P2
50 µm
DAPI FABP4 ARL13B
h
% Fabp4+ cells
0.0014
100
80
60
40
20
0
-20
P1
P2
i
FI
MI
TUG-891
P1
P2
50 µm
DAPI LD540
j
Adipogenic index (LD540+/DAPI+ area)
0.0103
0.0198
0.0017
P1
P2
2.5
2.0
1.5
1.0
0.5
0.0
FI
MI
TUG-891
+ - - + - -
- + + - + +
- - + - - +

Figure 1

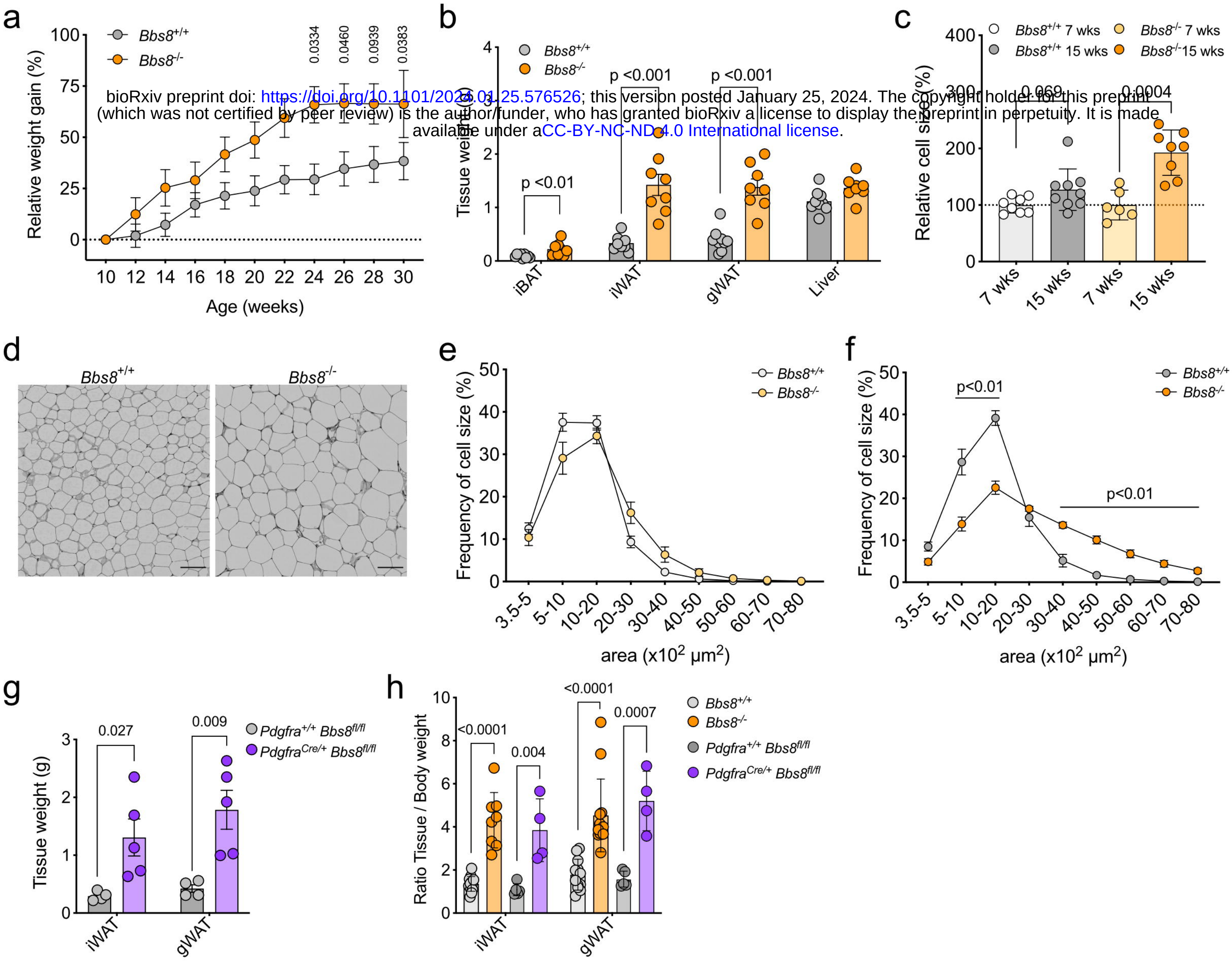
a
Relative weight gain (%)
100
75
50
25
0
Bbs8+/+
Bbs8-/-
0.0334
0.0460
0.0939
0.0383
10 12 14 16 18 20 22 24 26 28 30
Age (weeks)
b
Tissue weight (g)
4
3
2
1
0
Bbs8+/+
Bbs8-/-
p <0.01
p <0.001
p <0.001
iBAT
iWAT
gWAT
Liver
c
Relative cell size (%)
400
300
200
100
0
Bbs8+/+ 7 wks
Bbs8+/+ 15 wks
Bbs8-/- 7 wks
Bbs8-/-15 wks
0.069
0.0004
7 wks
15 wks
7 wks
15 wks
d
Bbs8+/+
Bbs8-/-
e
Frequency of cell size (%)
50
40
30
20
10
0
Bbs8+/+
Bbs8-/-
3.5-5
5-10
10-20
20-30
30-40
40-50
50-60
60-70
70-80
area (x10² µm²)
f
Frequency of cell size (%)
50
40
30
20
10
0
Bbs8+/+
Bbs8-/-
p<0.01
p<0.01
3.5-5
5-10
10-20
20-30
30-40
40-50
50-60
60-70
70-80
area (x10² µm²)
g
Tissue weight (g)
3
2
1
0
0.027
0.009
Pdgfra+/+ Bbs8fl/fl
PdgfraCre/+ Bbs8fl/fl
iWAT
gWAT
h
Ratio Tissue / Body weight
10
8
6
4
2
0
<0.0001
0.004
<0.0001
0.0007
Bbs8+/+
Bbs8-/-
Pdgfra+/+ Bbs8fl/fl
PdgfraCre/+ Bbs8fl/fl
iWAT
gWAT

Figure 2

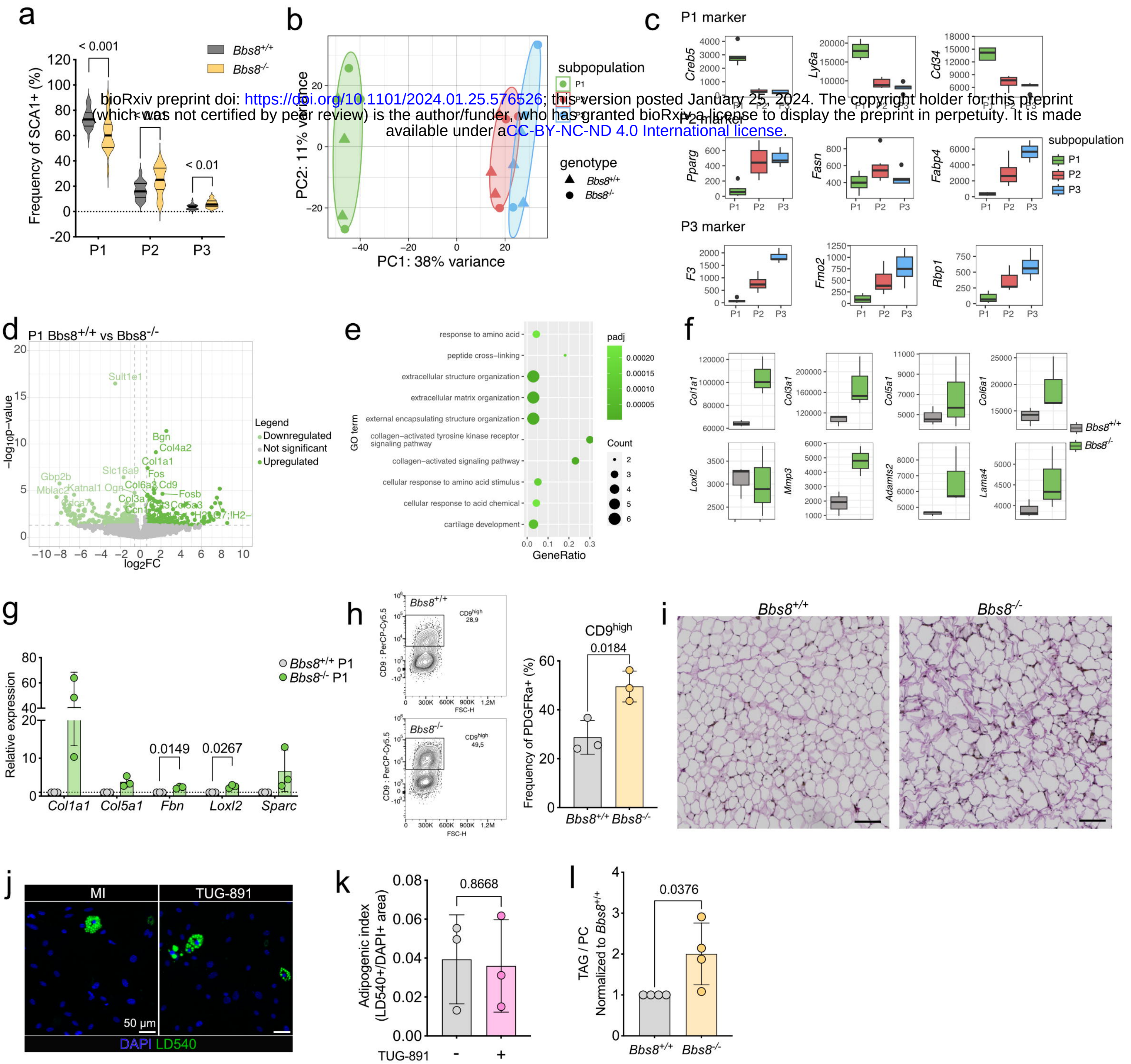
a
Frequency of SCA1+ (%)
< 0.001
< 0.01
Bbs8+/+
Bbs8-/-
P1
P2
P3
b
PC1: 38% variance
PC2: 11% variance
subpopulation
P1
P2
P3
genotype
Bbs8+/+
Bbs8-/-
c
P1 marker
Creb5
Ly6a
Cd34
P2 marker
Pparg
Fasn
Fabp4
P3 marker
F3
Fmo2
Rbp1
d
P1 Bbs8+/+ vs Bbs8-/-
-log10p-value
log2FC
Legend
Downregulated
Not significant
Upregulated
Sult1e1
Bgn
Col4a2
Col1a1
Fos
Gbp2b
Mblac2
Katnal1
Ogn
Slc16a9
Col6a3
Cd9
Fosb
Col3a1
Col5a3
e
GO term
response to amino acid
peptide cross-linking
extracellular structure organization
extracellular matrix organization
external encapsulating structure organization
collagen-activated tyrosine kinase receptor signaling pathway
collagen-activated signaling pathway
cellular response to amino acid stimulus
cellular response to acid chemical
cartilage development
GeneRatio
padj
Count
f
Col1a1
Col3a1
Col5a1
Col6a1
Loxl2
Mmp3
Adamts2
Lama4
Bbs8+/+
Bbs8-/-
g
Relative expression
Bbs8+/+ P1
Bbs8-/- P1
0.0149
0.0267
Col1a1
Col5a1
Fbn
Loxl2
Sparc
h
Bbs8+/+
Bbs8-/-
CD9 : PerCP-Cy5.5
FSC-H
CD9high 28,9
CD9high 49,5
CD9high
0.0184
Frequency of PDGFRa+ (%)
i
Bbs8+/+
Bbs8-/-
j
MI
TUG-891
50 µm
DAPI LD540
k
0.8668
Adipogenic index (LD540+/DAPI+ area)
TUG-891
-
+
l
0.0376
TAG / PC Normalized to Bbs8+/+
Bbs8+/+
Bbs8-/-

Figure 3

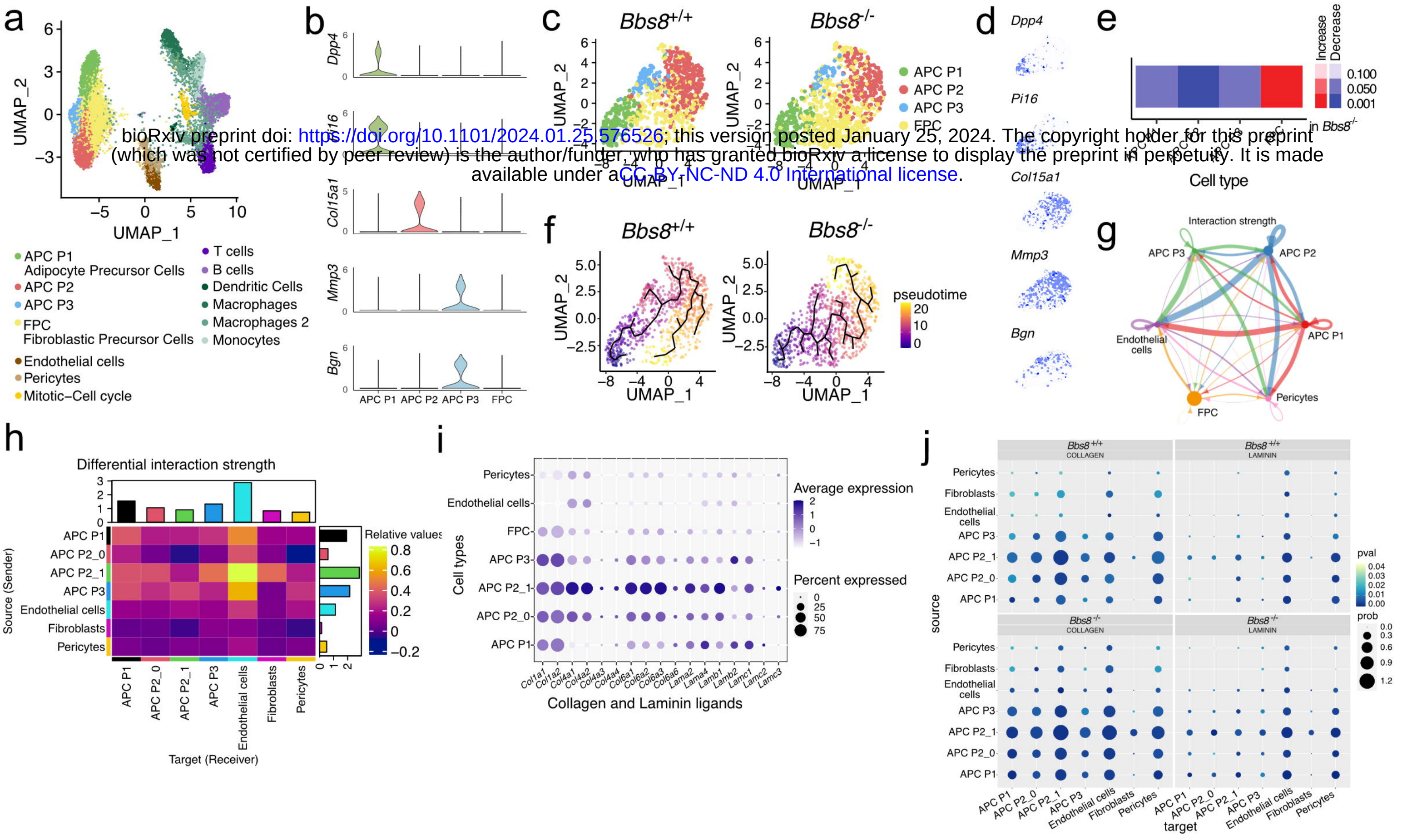
a
UMAP_1
UMAP_2
APC P1
Adipocyte Precursor Cells
APC P2
APC P3
FPC
Fibroblastic Precursor Cells
Endothelial cells
Pericytes
Mitotic−Cell cycle
T cells
B cells
Dendritic Cells
Macrophages
Macrophages 2
Monocytes
b
Dpp4
Pi16
Col15a1
Mmp3
Bgn
APC P1
APC P2
APC P3
FPC
c
Bbs8+/+
Bbs8-/-
UMAP_1
UMAP_2
APC P1
APC P2
APC P3
FPC
d
Dpp4
Pi16
Col15a1
Mmp3
Bgn
e
Increase
Decrease
0.100
0.050
0.001
in Bbs8-/-
Cell type
f
Bbs8+/+
Bbs8-/-
UMAP_1
UMAP_2
pseudotime
20
10
0
g
Interaction strength
APC P3
APC P2
Endothelial cells
APC P1
FPC
Pericytes
h
Differential interaction strength
Source (Sender)
Target (Receiver)
APC P1
APC P2_0
APC P2_1
APC P3
Endothelial cells
Fibroblasts
Pericytes
Relative values
0.8
0.6
0.4
0.2
0
−0.2
i
Cell types
Pericytes
Endothelial cells
FPC
APC P3
APC P2_1
APC P2_0
APC P1
Col1a1
Col1a2
Col4a1
Col4a2
Col4a3
Col4a4
Col6a1
Col6a2
Col6a3
Col6a6
Lama2
Lama4
Lamb1
Lamb2
Lamc1
Lamc2
Lamc3
Collagen and Laminin ligands
Average expression
2
1
0
−1
Percent expressed
0
25
50
75
j
Bbs8+/+
COLLAGEN
Bbs8+/+
LAMININ
Bbs8-/-
COLLAGEN
Bbs8-/-
LAMININ
source
target
pval
0.04
0.03
0.02
0.01
0.00
prob
0.0
0.3
0.6
0.9
1.2

Figure 4

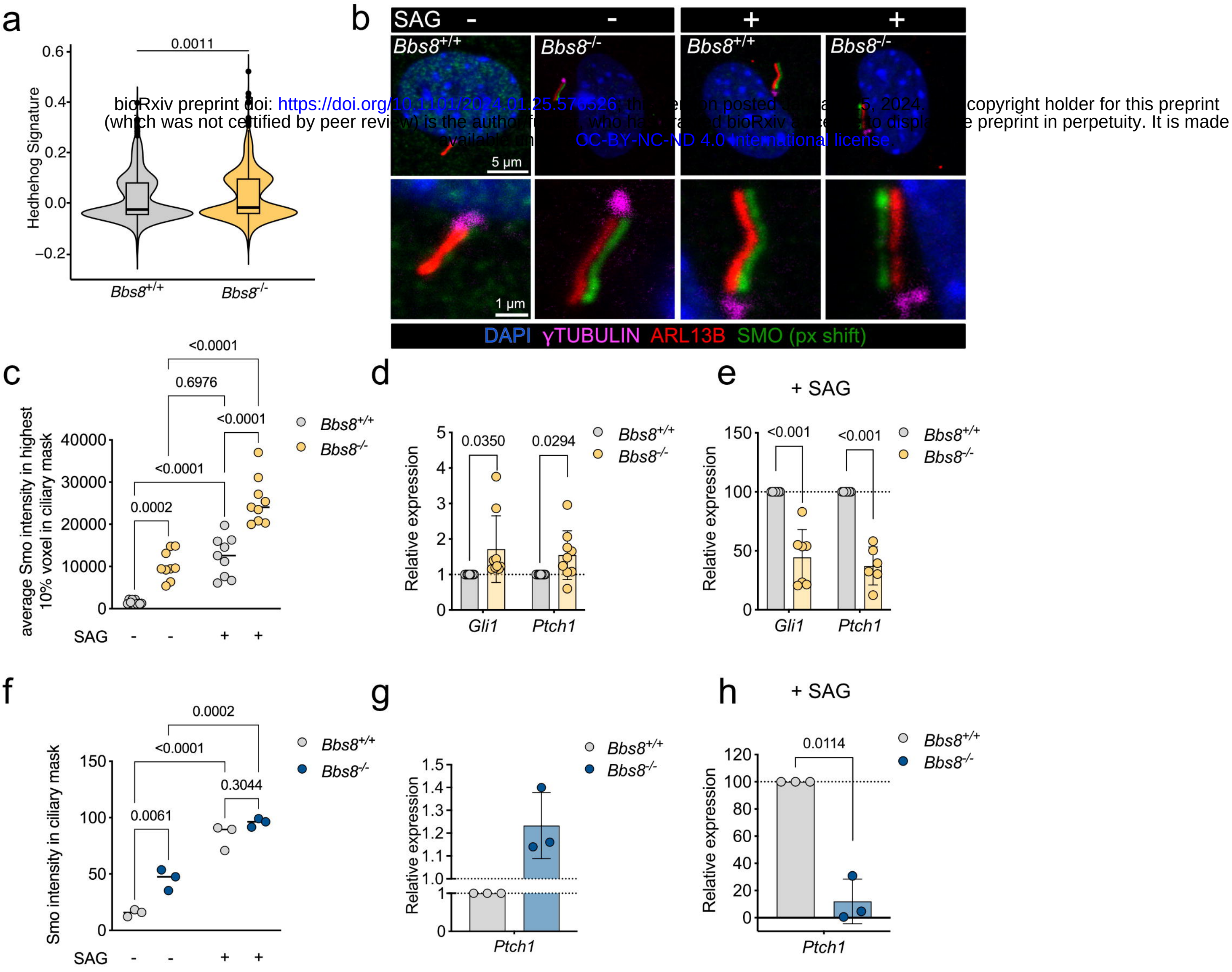
a
0.0011
Hedhehog Signature
0.6
0.4
0.2
0.0
−0.2
$Bbs8^{+/+}$
$Bbs8^{-/-}$
b
SAG - - + +
$Bbs8^{+/+}$
$Bbs8^{-/-}$
$Bbs8^{+/+}$
$Bbs8^{-/-}$
5 µm
1 µm
DAPI γTUBULIN ARL13B SMO (px shift)
c
<0.0001
0.6976
<0.0001
<0.0001
0.0002
average Smo intensity in highest 10% voxel in ciliary mask
40000
30000
20000
10000
0
SAG - - + +
$Bbs8^{+/+}$
$Bbs8^{-/-}$
d
0.0350
0.0294
Relative expression
5
4
3
2
1
0
Gli1
Ptch1
$Bbs8^{+/+}$
$Bbs8^{-/-}$
e
+ SAG
<0.001
<0.001
Relative expression
150
100
50
0
Gli1
Ptch1
$Bbs8^{+/+}$
$Bbs8^{-/-}$
f
0.0002
<0.0001
0.3044
0.0061
Smo intensity in ciliary mask
150
100
50
0
SAG - - + +
$Bbs8^{+/+}$
$Bbs8^{-/-}$
g
Relative expression
1.5
1.4
1.3
1.2
1.1
1.0
1
0
Ptch1
$Bbs8^{+/+}$
$Bbs8^{-/-}$
h
+ SAG
0.0114
Relative expression
120
100
80
60
40
20
0
Ptch1
$Bbs8^{+/+}$
$Bbs8^{-/-}$

Figure 5